



JGR Solid Earth

RESEARCH ARTICLE

10.1029/2019JB018053

Key Points:

- In Cascadia, differencing tidally filtered, depth-matched seafloor pressure records can reduce oceanographic noise to less than 1-cm RMS
- Models of offshore SSEs in Cascadia suggest that a network of depth-matched sensors at 30-km spacing can detect M_w 6.4 and larger events
- No offshore slow-slip earthquakes are detected in the available Cascadia seafloor pressure data from 2011 to 2015

Supporting Information:

- Supporting Information S1

Correspondence to:

E. K. Fredrickson,
erikfred@uw.edu

Citation:

Fredrickson, E. K., Wilcock, W. S. D., Schmidt, D. A., MacCready, P., Roland, E., Kurapov, A. L., et al. (2019). Optimizing sensor configurations for the detection of slow-slip earthquakes in seafloor pressure records, using the Cascadia Subduction Zone as a case study. *Journal of Geophysical Research: Solid Earth*, 124. <https://doi.org/10.1029/2019JB018053>

Received 16 MAY 2019

Accepted 8 DEC 2019

Accepted article online 11 DEC 2019

Optimizing Sensor Configurations for the Detection of Slow-Slip Earthquakes in Seafloor Pressure Records, Using the Cascadia Subduction Zone as a Case Study

Erik K. Fredrickson¹, William S. D. Wilcock¹, David A. Schmidt², Parker MacCready¹, Emily Roland¹, Alexander L. Kurapov³, Mark A. Zumberge⁴, and Glenn S. Sasagawa⁴

¹School of Oceanography, University of Washington, Seattle, WA, USA, ²Department of Earth and Space Sciences, University of Washington, Seattle, WA, USA, ³Coast Survey Development Laboratory, National Oceanic and Atmospheric Administration, Silver Spring, MD, USA, ⁴Institute of Geophysics and Planetary Physics, Scripps Institution of Oceanography, University of California, San Diego, La Jolla, CA, USA

Abstract We present seafloor pressure records from the Cascadia Subduction Zone, alongside oceanographic and geophysical models, to evaluate the spatial uniformity of bottom pressure and optimize the geometry of sensor networks for resolving offshore slow-slip transients. Seafloor pressure records from 2011 to 2015 show that signal amplitudes are depth-dependent, with tidally filtered and detrended root-mean-squares of <2 cm on the abyssal plain and >6 cm on the continental shelf. This is consistent with bottom pressure predictions from circulation models and comparable to deformation amplitudes from offshore slow slip observed in other subduction zones. We show that the oceanographic component of seafloor pressure can be reduced to ≤1-cm root-mean-square by differencing against a reference record from a similar depth, under restrictions that vary with depth. Instruments at 100–250 m require depths matched within 10 m at separations of <100 km, while locations deeper than 1,400 m are broadly comparable over separations of at least 300 km. Despite the significant noise reduction from this method, no slow slip was identified in the dataset, possibly due to poor spatiotemporal instrument coverage, nonideal deployment geometry, and limited depth-matched instruments. We use forward predictions of deformation from elastic half-space models and hindcast pressure from circulation models to generate synthetic slow-slip observational records and show that a range of slip scenarios produce resolvable signals under depth-matched differencing. For future detection of offshore slow slip in Cascadia, we recommend a geometry in which instruments are deployed along isobaths to optimize corrections for oceanographic signals.

Plain Language Summary Slow-slip earthquakes, a special class of earthquake in which slip along a fault occurs over periods of days to years without producing shaking, have increasingly been found to occur in the subsea segments of subduction zones worldwide. There is evidence that these offshore slow-slip earthquakes can occur within the same region where large, damaging earthquakes are generated and that they may precede and potentially trigger these events. Offshore slow-slip earthquakes cause the seafloor to move vertically by up to a few centimeters, which can be detected by measuring the pressure on the seafloor if the effects of ocean tides and circulation can be corrected for. In this study, we search for evidence of slow-slip earthquakes in seafloor pressure data from the Cascadia Subduction Zone, off the U.S. and Canadian west coast, and assess how to best reduce oceanographic signals in these data in order to reliably observe slow-slip deformation. No evidence for these events is seen in Cascadia pressure data from 2011 to 2015. Using a combination of observational data and model simulations, we show that oceanographic signals can be largely eliminated from seafloor pressure measurements if instruments are placed in rows of constant depth. A network of 22 instruments would be sufficient to monitor for large offshore slow-slip earthquakes offshore central Oregon, but smaller events would be difficult to detect with this method. By increasing our ability to detect these slow-slip earthquakes, we can better understand subduction zone processes and their relation to large, damaging megathrust earthquakes.

1. Introduction

Subduction zones are the sites of the world's largest earthquakes, with high potential for damaging shaking and tsunamigenesis. The locked region of subduction zones, where megathrust earthquakes occur, is often located offshore and has historically been difficult to observe. As such, the slip behavior of offshore seismogenic zones on subduction thrusts is not well understood. The archetypical subducting plate boundary is divided from depth to surface into a zone of stable sliding at depth, a transition zone of slow-slip earthquakes (SSEs) and tremor, a locked or partially locked seismogenic zone, and an uncoupled region extending up to the trench (e.g., Hyndman, 2013). This view has been amended in recent years to include, at some subduction zones, another transition zone updip of the seismogenic zone that hosts slow slip (shallow SSEs) and tremor (Araki et al., 2017; Obara & Kato, 2016). However, it is not known if these features are ubiquitous or particular to specific subduction regimes. Resolving this ambiguity has important implications for subduction zone hazards, particularly the determination of likely megathrust rupture locations and tsunami amplitudes, as interseismic deformation will influence stress accumulation and potentially coseismic displacements on the updip edge of the megathrust.

SSEs downdip of the seismogenic zone have been well studied in subduction zones worldwide, particularly in Nankai (Hirose et al., 1999; Obara, 2002), Cascadia (Dragert et al., 2001), Costa Rica (Dixon et al., 2014), New Zealand (Wallace & Beavan, 2010), and Mexico (Lowry et al., 2001). During slow slip, displacement occurs along the fault over much longer periods of time than in a normal earthquake. Although they vary in size, SSEs are capable of releasing considerable strain energy, up to M_w 7.0 or greater (Schwartz & Rokosky, 2007). SSEs sometimes occur in the same fault region as tremor and low-frequency earthquakes, though they are not always found concurrently (Rogers & Dragert, 2003; Shelly et al., 2007) and the updip extent of slow slip may consistently occur beyond that of tremor (Hall et al., 2018; Wang et al., 2008). SSEs appear to obey scaling laws akin to, but different from, those of regular earthquakes, including a relationship between seismic moment and fault area in which stress drops are generally found to be between 0.01 and 0.10 MPa (Gao et al., 2012), though there are exceptions above and below this range (e.g., Brodsky & Mori, 2007). There is also evidence that SSE and regular earthquakes obey the same moment-duration scaling, which is bimodal as a function of slip area (Gomberg et al., 2016). SSE durations vary broadly, ranging from days to years, leading to the categorization of long-term and short-term events (Fu & Freymueller, 2013; Radiguet et al., 2011).

In the past decade, studies in other subduction zone settings that incorporate offshore measurements, such as seafloor pressure, borehole formation pressure, or ocean bottom seismometers (Araki et al., 2017; Davis et al., 2015; Ito et al., 2013; Wallace et al., 2016), or where the trench is in close proximity to land (Dixon et al., 2014; Ozawa et al., 2007; Radiguet et al., 2016; Ruiz et al., 2014; Vallée et al., 2013; Wallace & Beavan, 2010) have identified shallow SSEs within and updip of the seismogenic zone. Measuring SSE signals on the seafloor is challenging, as there is added difficulty in instrument design and deployment, and the ocean is a significant source of noise. Nonetheless, some of those events successfully observed show consistency in fault size, slip magnitude, and duration. Shallow SSEs recorded on seafloor pressure instruments in Hikurangi (Wallace et al., 2016) and the Japan Trench (Ito et al., 2013) measured 1.5- to 6-cm vertical deformation at the seafloor over periods of 1–2 weeks and areas of 40–60 km across-strike and 75–80 km along-strike, which were inverted for 10- to 25-cm peak slip at depths of 15 km up to the trench. The Japan Trench SSEs were separated by 27 months, while Hikurangi shallow SSEs have been observed in the onshore geodetic record to recur at intervals of 18–24 months (Wallace et al., 2012). Davis et al. (2015) used borehole and seafloor pressure to identify near-trench slow slip near Costa Rica's Nicoya Peninsula with comparable vertical deformation, but with only two instrument sites could not infer detailed fault parameters.

Similarly, repeating shallow SSEs have been identified in offshore borehole pressure and low-frequency tremor records in the Nankai Subduction Zone (Araki et al., 2017). These events seem to occur over smaller areas, typically 20–40 km, and produce less deformation. The existence of such low-magnitude SSEs suggests the possibility of their occurrence elsewhere and motivates the development of improved observational methods and techniques for increasing detection capabilities. Yamashita et al. (2015) also measured a shallow, migrating tremor episode in southern Japan on an ocean bottom seismometer network and inferred a coincident SSE with an along-strike extent of up to 150 km. There is global evidence that these shallow slip processes may be capable of triggering megathrust earthquakes (Ito et al., 2013; Kato et al., 2012; Ruiz et al., 2014; Uchida et al., 2016).

The Cascadia Subduction Zone exists between the North American Plate and the converging Juan de Fuca Plate, which subducts obliquely at a variable rate that increases from 3.0 cm/year off California in the south to 4.5 cm/year off Vancouver Island in the north (Schmalzle et al., 2014). This subduction zone has historically produced $M_w \sim 9.0$ megathrust earthquakes with a recurrence interval of ~500 years (Atwater, 1987), the last of which occurred in 1700 (Atwater et al., 2015). Sedimentary records indicate that smaller ($M_w \sim 8$), partial ruptures occur more frequently in the south, at an interval of ~240 years (Goldfinger et al., 2012). As such, the Cascadia Subduction Zone poses a significant seismic hazard to western U.S. and Canadian regions.

There is limited information in Cascadia regarding the presence or absence of SSEs and tremor updip of the seismogenic zone. Current land-based seismic and geodetic measurements are not able to fully resolve the state of locking in the offshore segment of the subduction zone (Wang & Tréhu, 2016), though there are indications that there is a lesser degree of locking offshore northern and central Oregon (Burgette et al., 2009; Schmalzle et al., 2014). Until recent ocean-bottom instrument deployments, such as the Cascadia Initiative (CI; Toomey et al., 2014) and SeaJade experiment (Scherwath et al., 2011), information on seismicity was also limited. One recent study combining onshore and CI seismic data identified several hundred earthquakes between 2011 and 2015 of $M_w < 4$ (most less than 2) in the vicinity of the megathrust, which may provide additional constraints on locking (I. Stone, Vidale, et al., 2018). Increased offshore observations would provide a better understanding of the stress state of the subduction zone and possibly give clues as to where the next megathrust earthquake may occur.

In the Cascadia Subduction Zone, though we lack any information about offshore slip processes, a range of recurrence behavior is observed in the record of downdip SSEs. There is significant along-strike segmentation in recurrence interval, which is approximately 10 months beneath northern California, 19 months beneath central and northern Oregon, and 14 months beneath Washington and Vancouver Island (Brudzinski & Allen, 2007). This segmentation in Cascadia is manifested in other properties of the subduction zone (e.g., Porritt et al., 2011) and may also apply to any shallow SSE behavior. There is also across-strike variation in slip behavior, with smaller, more frequent events occurring further downdip and larger, less frequent events occurring further updip (Wech & Creager, 2011).

Offshore instrumentation is important for the measurement of shallow SSEs in Cascadia because the large distance between shoreline and trench (from ~90 km in the south to >150 km in the north) limits the detection of offshore deformation and seismicity by onshore Global Positioning System (GPS) and seismometers. Seafloor absolute pressure gauges (APGs) provide a measure of the overlying atmospheric and oceanic mass and are therefore sensitive to the vertical deformation of the seafloor from SSEs. The major contributions to seafloor pressure are the average water depth, tides, nontidal oceanographic effects, and geophysical signals. Quartz pressure sensors, which produce high-resolution data, are subject to an instrumental drift that adds an additional term to the measured pressure. This drift can be fit with an initial exponential term that has a characteristic time of weeks to months superimposed upon a linear trend (Polster et al., 2009; Watts & Kontoyiannis, 1990). To isolate the geophysical signals, pressures from APGs are generally filtered for tides, detrended for sensor drift, then subjected to station differencing, wherein a reference pressure record is subtracted from all others (e.g., Wallace et al., 2016). This reference, located away from the deformation, is assumed to capture the regional oceanographic pressure signal, and after its subtraction any remaining signals are assumed attributable to vertical geophysical deformation.

In this paper, we search for evidence of offshore SSEs in the available Cascadia seafloor pressure data between 2011 and 2015, present a method for best reducing oceanographic pressure signals, and assess the sensitivity of APGs to the deformation signals produced by SSEs, using data from seafloor sensors and models of oceanographic circulation and crustal deformation. We assess the spatial scales of significant oceanographic noise reduction in these data and models to infer the optimal sensor configurations for the purpose of detecting SSEs in the offshore setting.

2. Methods

2.1. APG Data

We use data from seafloor APGs deployed between 2011 and 2015 (Figure 1) to search for evidence of SSEs in Cascadia. The bulk of these data come from the CI experiment (Toomey et al., 2014), an ocean bottom

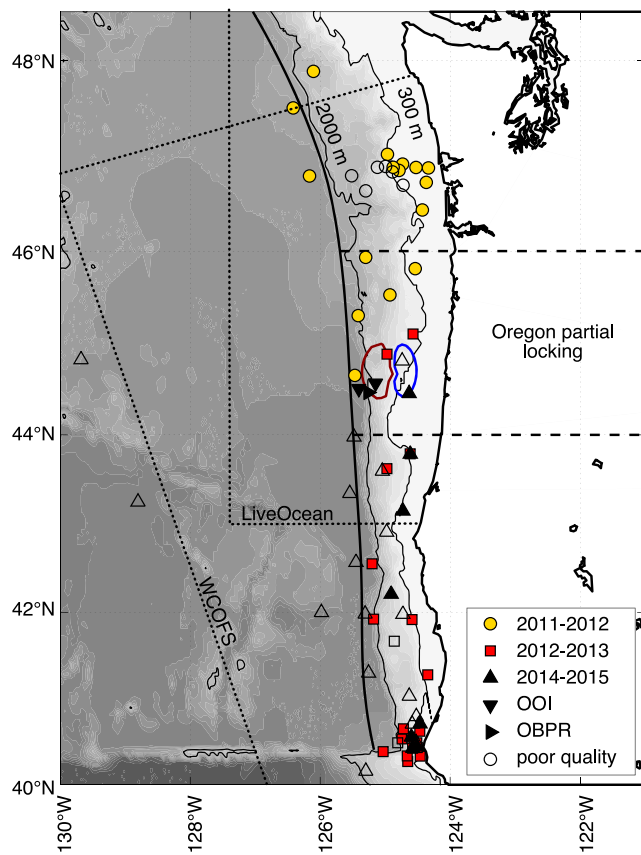


Figure 1. Map of the study area, depicting bathymetry, and station locations. The thin black contours at 300- and 2,000-m differentiate near-shelf, slope, and abyssal plain regimes, the dotted lines show the LiveOcean and West Coast Ocean Forecast System (WCOFS) model domains, the black bold line depicts trench axis as per McCrory et al. (2012), and the dashed black lines at 44 and 46°N depict the approximate bounds of the region of partial locking offshore northern Oregon (Burgette et al., 2009; Schmalzle et al., 2014). Pressure gauge instrument locations are displayed with symbols and colors corresponding to experiment years and are unfilled for those which did not yield useable data. The 2013–2014 experiment year is excluded because it had only one useable quality station. The 2014–2015 instruments include cabled pressure gauges from the OOI Cabled Array and a benchmark sensor offshore central Oregon (OBPR), which are denoted by rotated triangles. The red and blue contours show the 1.5-cm uplift and subsidence areas, respectively, from our base slow-slip earthquake model.

seismometer deployment aimed at recording regional and teleseismic earthquakes on the Juan de Fuca plate and Cascadia forearc. Instruments were recovered and replaced each summer, alternating between northern ($>44^{\circ}\text{N}$) and southern locations ($<45^{\circ}\text{N}$) every year. This results in the division of these data into the experiment years 2011–2012, 2012–2013, 2013–2014, and 2014–2015. The experiment was not designed with the purpose of detecting offshore SSEs, so deployment geometries were not idealized for this purpose. A total of 70 instruments were used for this experiment. All the instruments had four channels: a three-component seismometer and a fourth channel to measure pressure. The fourth channel for 40 instruments from Scripps Institution of Oceanography and Woods Hole Oceanographic Institution was equipped with a differential pressure gauges (Cox et al., 1984), which could not be used in this study due to their inability to measure pressure changes at periods greater than $\sim 1,000$ s. The remaining 30 instruments from Lamont-Doherty Earth Observatory used Paroscientific resonant quartz crystal APGs. Of these, 20 were specifically designed with trawl-resistant housings and deployed at depths less than 1,000 m. The CI APGs collected data at 125 Hz, which we down-sampled to 1 sample/hr with a zero-phase filter before performing our analysis. APGs on the Ocean Observatories Initiative (OOI) Cabled Array (Smith et al., 2018) and a pressure benchmark from offshore central Oregon (Cook et al., 2017) provide additional data in the 2014–2015 year.

In total, there are 16 pressure records useable for this study in 2011–2012, 19 in 2012–2013, and 11 in 2014–2015. No useable data was recorded in 2013–2014. Data quality issues associated with the excluded instruments are discussed in Text S1 in the supporting information. Many of the instruments in each year are located on or near the continental shelf (defined here as depth <300 m): 9 in 2011–2012, 8 in 2012–2013, and 7 in 2014–2015. Few instruments are located on the continental slope (defined here as 300 m < depth < 2,000 m): 3 in 2011–2012, 8 in 2012–2013, and 2 in 2014–2015. The remaining 4, 3, and 2 instruments in each year are located on or near the abyssal plain (defined here as depth >2,000 m).

To recover the geophysical signals from these data, the highest amplitude portion of exponential sensor drift was removed by discarding the first 2 weeks of data. The pressure records were then detided using a low-pass Godin filter, in which three running averages are applied at 24, 24, and 25 hr (Emery & Thomson, 2004; Godin, 1972), and a third-order polynomial was fit and subtracted from each time series to remove the mean and any long-period signal. A polynomial of third order, the minimum to remove the seasonal signal seen in many oceanographic observables (e.g., Giddings et al., 2014), was chosen to balance root-mean-square (RMS) reduction and the risk of overfitting, including the fitting of any transient deformation signal (see Text S2 and Figure S1 in the supporting information). These processed data are shown in Figure 2. Here and throughout this paper, changes in pressure are given in equivalent centimeters of seawater (at $\rho = 1,026 \text{ kg/m}^3$). Detided and polynomial-corrected pressure time series were then analyzed for SSEs by using station differencing and by inspecting visually for steps that might be due to deformation.

2.2. Physical Oceanographic Circulation Models

To better understand the effects of physical oceanographic processes on seafloor pressure, and to assess the effectiveness of station differencing, we utilized two ocean circulation models that overlapped our study region, the domains of which are shown in Figure 1. One is the LiveOcean model developed by the University of Washington Coastal Modeling Group (Giddings et al., 2014; H. B. Stone, Banas, & MacCready, 2018), which extends from 43 to 50°N. The other is the West Coast Ocean Forecast System (WCOFS) developed at the National Oceanic and Atmospheric Administration (NOAA) Coast Survey Development Laboratory (Kurapov et al., 2017), which extends along the North American coast from 24 to 54°N. The LiveOcean model has 1.5-km resolution near the coast, decreases to 4.5-km resolution offshore, and at all points has 40 vertical layers optimized for determining surface and bottom conditions. The WCOFS model has a uniform 2-km resolution with 40 vertical layers, at least 10 of which are in the top 50 m of the water column. Both models are constructed using the Regional Ocean Modeling System (ROMS) framework, which uses the seawater equation of state and conservation of tracers, within the Boussinesq approximation. The pressure is hydrostatic, and equations are solved to generate full 3-D fields of physical oceanographic parameters, optimized for integrated conservation, and constancy preservation given a free ocean surface and realistic bathymetry (Shchepetkin & McWilliams, 2005). Forcings come from atmospheric, tidal, and river inputs, in addition to model boundary conditions from the U.S. Navy HYCOM (Chassignet et al., 2007). The calculated fields are validated against observational data, including temperature, salinity, and tide gauges.

Such models are typically used to study regional ocean circulation processes, such as major currents or regions of upwelling, that can be tied to the transport of biological and chemical tracers of interest. These models were not developed for the purpose of calculating seafloor pressure, but they contain the necessary fields to do so. Global-scale barotropic models have previously been used to this end (Inazu et al., 2012; Ito et al., 2013; Muramoto et al., 2019). Herein, modeled bottom pressures were calculated hourly, averaged daily, and subjected to the same filtering and polynomial fitting as the APG data to ensure comparability. We use the LiveOcean model from January 2013 (its inception) to December 2015 (the end of our APG dataset) and the WCOFS model from January 2011 (the start of our APG dataset) to December 2014 (its latest available date). The combined spatiotemporal model domain overlaps with all but one instrument in the 2011–2012 and 2012–2013 APG datasets but provides only partial spatial overlap with the 2014–2015 data. Though the two models show some differences in their common year (2013–2014), particularly off the continental shelf, we determine that they predict bottom pressures similar enough to be used interchangeably (see Text S3 and Figures S2–S4).

We quantified the comparability between models and data by calculating the R^2 of the fit of the modeled bottom pressure to the observed pressure at the same location, given by

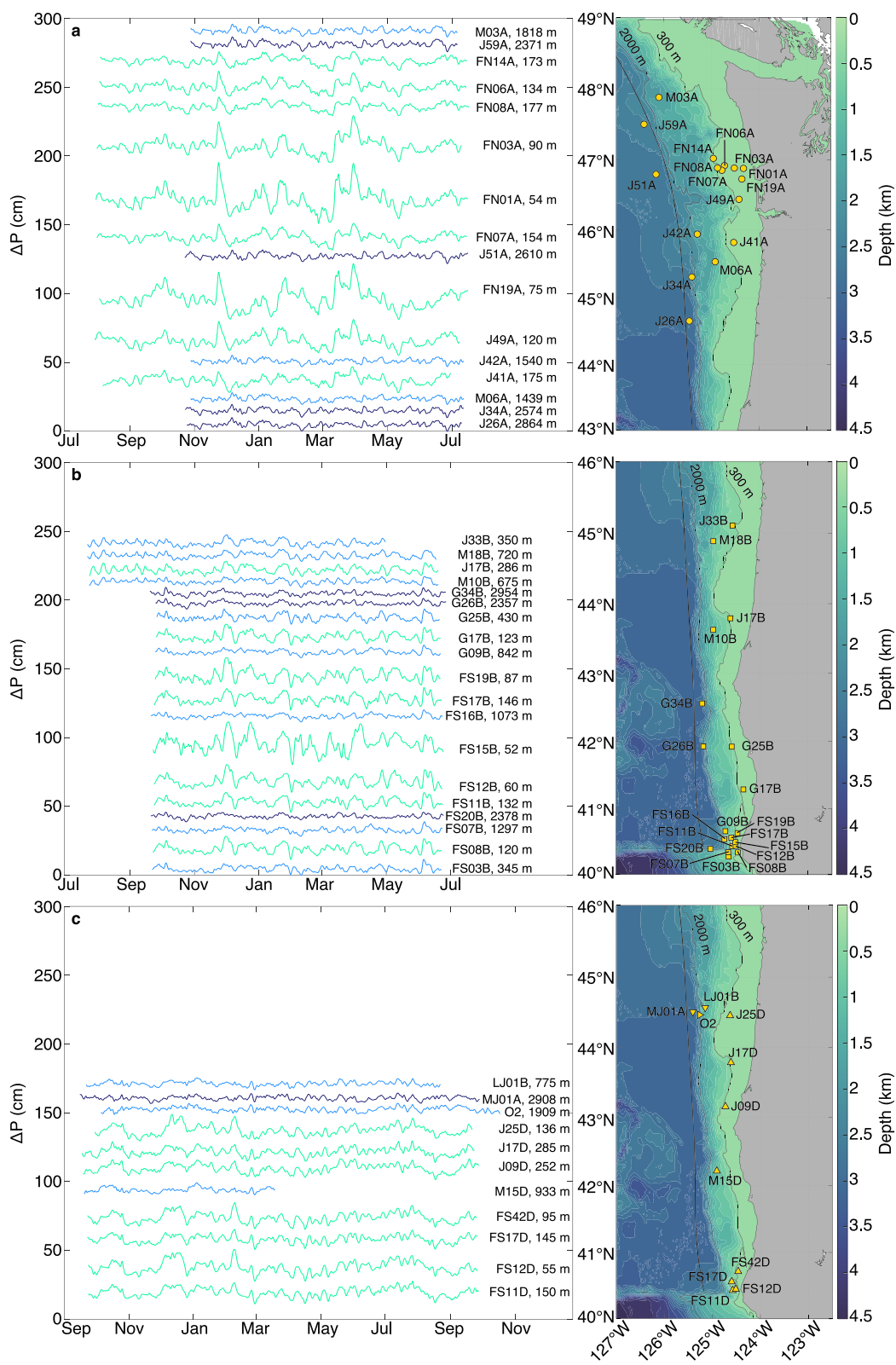


Figure 2. The pressure data used in these analyses, offset for display purposes, alongside maps of instrument locations for (a) 2011–2012, (b) 2012–2013, and (c) 2014–2015. For each time series, the first 2 weeks of data are discarded, a Godin 24-24-25 filter (Godin, 1972) is applied, and a third-order polynomial fit is removed. Data from below 2,000-m depth are plotted in dark blue, depths 300–2,000 m in light blue, and depths above 300 m in green. Station name and depth are listed next to each time series. The start and end times of the data vary, according to deployment/recovery and scheduled ship time.

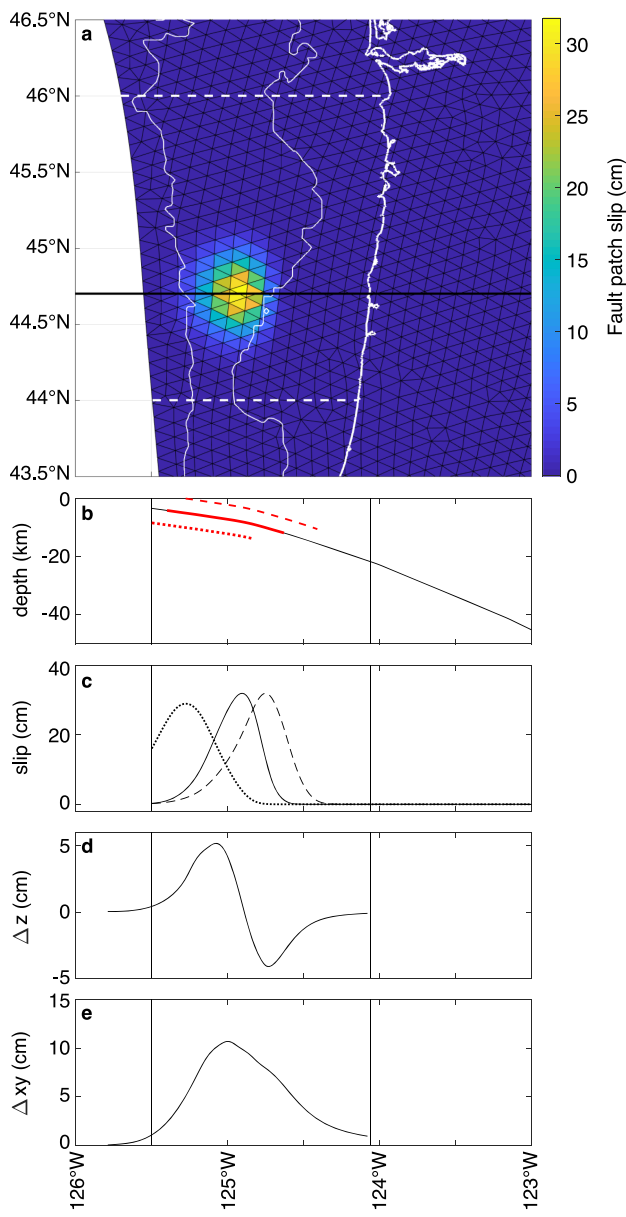


Figure 3. (a) Parameterization of the Juan de Fuca slab surface into triangular elements, used in our deformation modeling, with elements color coded according to slip amplitude for the base model. The trench is depicted by the westernmost boundary of the slab, the coastline is shown in bold white, the thin white contours show 300- and 2,000-m depth, and the dashed white lines at 44 and 46°N depict the approximate bounds of the region of partial locking offshore northern Oregon (Burgette et al., 2009; Schmalzle et al., 2014). The black line at 44.7°N indicates the cross section line for (b)–(e). (b) Cross section of plate interface depth versus longitude with the region of slip highlighted in red. The dotted and dashed red curves below and above show the slip region for updip and downdip model variations, respectively, offset vertically for display purposes. Note that depth is given relative to the seafloor and does not go to zero at the trench due to significant sediment coverage in Cascadia. (c) Slip versus longitude, with updip and downdip variations shown by dotted and dashed curves, respectively. (d) Surface vertical deformation versus longitude. (e) Surface horizontal deformation versus longitude. Vertical bars in (b)–(d) represent the locations of the deformation front and coastline in the cross-section.

$$R^2 = 1 - \frac{\sigma_{y-x}^2}{\sigma_y^2} \quad (1)$$

where σ_y^2 is the variance in the observed data and σ_{y-x}^2 is the variance in the model-corrected signal. This relation is similarly used to assess the agreement of the two models. As the relationship between the model and observations is nonlinear, the calculated R^2 values do not have an easily interpretable meaning (e.g., Kvamseth, 1985) but do provide a quantitative assessment of the goodness of fit at a given location and can be compared to one another. A positive R^2 signifies that variance is reduced by differencing, while a negative R^2 signifies that variance is increased.

2.3. Geophysical Slow-Slip Modeling

We also present elastic slip models of representative SSEs to understand the nature of expected signals in the region and the ability of an APG network to detect them. We model the Cascadia Subduction Zone fault surface as 5,729 planar, triangular elements following the slab model of McCrory et al. (2012), adjusting depth to be relative to the seafloor rather than to sea level, as shown in Figure 3. Green's functions were then calculated for each element in an elastic half-space using the boundary element code Poly3D (Thomas, 1993), allowing the determination of vertical displacement, among other parameters, for a given slip geometry. We use a Poisson's ratio of $\nu = 0.38$ and a Shear Modulus of $\mu = 10$ GPa, consistent with the physical properties of the accretionary prism (Jeppson et al., 2018). Modeled displacements are incorporated into modeled oceanographic bottom pressure time series from LiveOcean to generate synthetic time series of various SSE scenarios in Cascadia from which detectability can be assessed. These synthetics were detided and corrected with a third-order polynomial after incorporating SSE displacement, but before differencing, to mimic the handling of real observational data. Though not the focus of this study, we also assess detectability from on-land GPS by calculating predicted horizontal deformation at the coast. These predictions should be viewed as coarse approximations because our modeling space does not account for the complex structure and associated rheological changes at and near the coast.

Slip geometries were based on measurements of offshore SSEs in other settings, predominantly Ito et al. (2013) and Wallace et al. (2016), who report M_w 6.8 events near the Japan and Hikurangi trenches, respectively. Spatial extents of both are elongated along-strike compared to across-strike, though the Japan trench event is not as well constrained along-strike due to the deployment geometry of that experiment. Neither SSE has a reported stress drop, but from the information provided for each an approximate value of $\Delta\sigma = 0.1$ MPa can be calculated. Given earthquake scaling laws, smaller events likely occur more regularly, but there are limited reports of smaller offshore SSEs in the literature, likely due to the difficulty in detecting these events. Araki et al. (2017) report offshore SSEs in Nankai of M_w 5.0–5.6, with displacement inferred from borehole formation pressures and spatial extent inferred from concurrent tremor. Other small-amplitude shallow SSE signals have been reported from borehole pressure measurements (e.g., Davis et al., 2015), but limited instrument coverage inhibits inferences about event size.

The base slip geometry used in our model is a two-dimensional Gaussian with 32-cm peak slip, constrained by depth and length along strike and

Table 1
Slow-Slip Earthquake Modeling Scenarios

Model Name	M_w	$\Delta\sigma_E$ (MPa)	$\Delta\sigma_M$ (MPa)	Dist. to shore (km)	L (km)	W (km)	Max slip (cm)	Δz_{\max} (cm)	Δz_{\min} (cm)	$L_{+\Delta z}$ (km)	$W_{+\Delta z}$ (km)	$L_{-\Delta z}$ (km)	$W_{-\Delta z}$ (km)	Δx_{coast} (cm)
Base (Figure 9)														
Time shifted (Figure S5)	6.4	0.057	0.031	72	96	60	32	5.5	-4.1	65	36	61	26	0.9
30 days (Figure S6)														
Near-trench (Figure 10)	6.4	0.057	0.036	100	90	55	28	5.1	-2.8	56	30	48	24	0.3
Near-shelf (Figure S7)	6.4	0.057	0.029	58	89	62	31	6.8	-3.9	67	38	60	27	1.7
Low $\Delta\sigma$ (Figure 11)	6.4	0.014	0.010	72	248	51	11	2.0	-1.7	80	18	52	7	0.5
High $\Delta\sigma$ (Figure S8)	6.4	0.217	0.104	72	37	62	78	10.6	-7.1	40	44	43	31	1.0
Low M_w (Figure 12)	5.9	0.022	0.016	72	65	47	9	1.5	-1.1	1	1	--	--	0.2
High M_w (Figure S9)	6.9	0.057	0.026	72	342	70	65	12.0	-9.9	240	48	237	43	3.4
Very low slip (Figure S10)	6.2	0.006	0.005	137	260	45	4	0.8	-0.5	--	--	--	--	0.1

Note. M_w : moment magnitude; $\Delta\sigma_E$: energy averaged stress drop; $\Delta\sigma_M$: moment-based stress drop; Dist. to shore: E-W distance from site of peak slip to shoreline; L: N-S total length of slip region; W: E-W total width of slip region; Max slip: maximum slip; Δz_{\max} : peak uplift at seafloor; Δz_{\min} : peak subsidence at seafloor; $L_{+\Delta z}$: N-S length of uplift $\geq 1.5\text{cm}$; $W_{+\Delta z}$: E-W width of uplift $\geq 1.5\text{cm}$; $L_{-\Delta z}$: N-S length of subsidence $\leq -1.5\text{cm}$; $W_{-\Delta z}$: E-W width of subsidence $\leq -1.5\text{cm}$; Δx_{coast} : horizontal displacement at the coast

centered beneath the continental slope offshore central Oregon (Figure 3a and Table 1), chosen for the inferred partial locking there (Burgette et al., 2009; Schmalzle et al., 2014). The Gaussian has a 19-km halfwidth in the north-south direction and 1.5-km halfwidth in the z direction (approximately corresponding to an east-west halfwidth of 12 km). To reduce the effects of our models' smoothness, which causes many elements to have very small, nonzero slip, in all models we reassign elements with $<1\text{cm}$ slip to instead have zero slip. The peak uplift generated by this event is 5.5 cm, consistent with values measured in Hikurangi and the Japan Trench. The fault slip in this setting corresponds to a minimum recurrence interval of 8.4 years, given the convergence rate of 3.8 cm/year at this location. We chose the slip to occur uniformly over 14 days, based off observations elsewhere. Our model results in a M_w 6.4 event, lower than reported in Hikurangi and Japan, a result of the significantly lower Shear Modulus used in our modeling, which was selected to accurately reflect the low rigidity of Cascadia's accretionary prism, while inversion modeling in Hikurangi and the Japan Trench assumed parameters consistent with continental crust.

We recognize that there is ambiguity in calculating the stress drop for a heterogeneous slip distribution (Noda et al., 2013). Herein, we present stress drops using the energy-based averaging approach of Noda et al. (2013, equation 10), which in the case of our discretized fault model is given by

$$\Delta\sigma_E = \frac{\sum \sigma_i D_i A_i}{\sum D_i A_i} \quad (2)$$

where $\Delta\sigma_i$, D_i , and A_i are the stress drop, slip, and area of a given patch, respectively, and the sum is performed over all slipping patches. However, much of the literature for recorded SSEs report a simplified stress drops that assumes an average slip over the entire slipping area, analogous to the moment-based approach Noda et al. (2013, equation 4), so in Table 1 we also report this value. In the text, we will explicitly denote each calculation as $\Delta\sigma_E$ and $\Delta\sigma_M$. This allows us to most accurately describe the nature of the slip distribution in our models while still giving a meaningful comparison to the literature (e.g., Gao et al., 2012). Our base model results in a stress drop of $\Delta\sigma_E = 0.057$ MPa, lower than estimated for Hikurangi and Japan due to our use of smaller elastic parameters.

To investigate a broader range of potential SSE behavior, we consider additional models in which we change the timing and duration of slip to reflect the broad range of observations elsewhere, the slip location along dip to explore trenchward and landward deformation, the stress drop to simulate end-members of a given moment release, and the moment magnitude to assess how observational parameters scale.

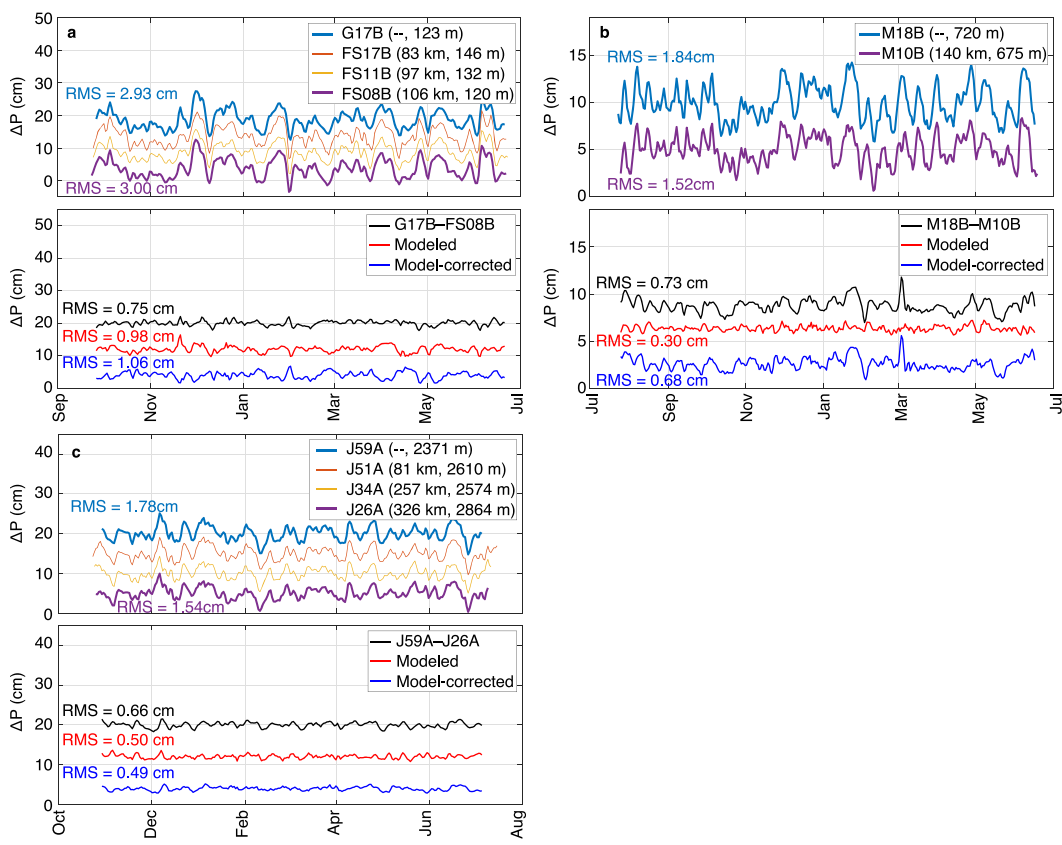


Figure 4. Example comparisons (upper panels) and differences (lower panels) of absolute pressure gauge (APG) time series at similar depths. (a) Comparison of continental shelf stations from 2012 to 2013. (b) Comparison of continental slope stations from 2012 to 2013. (c) Comparison of stations on the abyssal plain from 2011 to 2012. The legend in the upper panels indicates the names of instruments, their separation from the topmost instrument, and the water depth of their location. The bold curves indicate the two stations used to generate the differences in the lower panels. In the difference plots, the black curve depicts the time series obtained by differencing the APG data, the red curve depicts the difference from the West Coast Ocean Forecast System (WCOFS) model at the same locations, and the blue curve depicts the difference obtained after correcting the data with the model. Root mean squares (RMS) are listed for each. All curves are offset for display purposes. Instrument locations are mapped in Figure 2.

3. Results

3.1. Differencing of APG Data

The detided and polynomial-corrected APG data used in our study, shown in Figure 2, have signal amplitudes that decrease with water depth, from a mean of 5-cm RMS over the deployment interval for instruments at depths shallower than 100 m down to a mean of 1.5-cm RMS for instruments at depths below 1,400 m. The largest amplitudes come from the shallow, northern APGs in 2011–2012, with RMS ~1 cm larger than southern instruments from 2012 to 2013 and 2014 to 2015 at comparable depths. Pressure amplitudes increase in the winter across all stations and years, but the difference is most pronounced for shallow locations.

With the limited number of available instruments in each year, it was possible to apply station differencing to every combination of pressure time series. In all of the differences generated, no static step clearly indicative of SSE-induced deformation was found; however, the residual oceanographic noise varied greatly among these differences, from <1- to >7.5-cm RMS, so detectability varied similarly. The greatest reduction in nontidal oceanographic signal was achieved by differencing instruments at comparable depths. Examples of bottom pressure time series for instruments with comparable depths are shown in the upper panels of Figure 4, and their differences are shown as black curves in the lower panels. Inspected visually, the pressure time series at each depth show a high degree of similarity, and upon differencing, residual RMS of these examples are <1 cm. The differences do not, generally, have consistent RMS through time but instead have discrete segments of increased amplitude, on time scales of weeks.

Table 2 gives the RMS of differences for all groups of two or more stations at similar depths throughout experiment years, relative to the northernmost or southernmost station in the group. This was done to provide a representative range of separations and to minimize redundant information. A comprehensive list of all difference combinations for instruments at similar depths is given in Table S1 in the supporting information. In Figure 5 we explore all of the matched-depth differences further by separating instruments into depth bins and plotting the difference RMS between pairs of sensors versus the depth difference and lateral distance between sensors. These bins contain 25 differences at depth > 1,400 m (Figure 5a); 11 at 1,400 m > depth > 500 m (Figure 5b); 7 at 500 m > depth > 250 m (Figure 5c); 24 at 250 m > depth > 100m (Figure 5d); and 7 at depth < 100 m (Figure 5e) and were selected because the differences of instruments between bins had uniformly high RMS, in part because the depths are not evenly distributed within those bins. With the notable exception of instruments at <100-m depth, the majority of the depth-matched differences at separations <100 km from Figure 5 and Table 2 have \leq 1-cm RMS. We therefore find a vertical deformation amplitude of 1.5 cm to be an unambiguous SSE detection threshold for this dataset and use this threshold in the subsequent geophysical modeling scenarios.

3.2. Hindcast Seafloor Pressure From Circulation Models

The LiveOcean and WCOFS oceanographic models were used to assess how patterns identified in the APG dataset scale to a regional coverage area. Figure 6a contours bottom pressure RMS for all grid points in the WCOFS model for the 2013–2014 year, showing significant depth dependence for locations above midslope depths of about 1,000 m. This depth dependence is comparable to the scaling identified in the APG data: for the same APG locations shallower than 100m, the model predicts a mean 4-cm RMS, while for the same locations below 1,400 m, the model predicts a mean of 1.5 cm. Shallow, northern locations have the highest RMS, just as with the APG data.

Select pressure time series from the WCOFS oceanographic model are shown alongside pressure data from collocated CI APGs in Figure 7. The model accurately captures certain elements of the measured seafloor pressure signal, particularly in shallow, near-shore locations, as can be seen in the time series plotted in the upper panels of Figures 7a–7c, but consistently underpredicts RMS. The longest- and shortest-period pressure signals are generally well predicted, but those in the days to weeks range do not match the APG data well. This results in differences between observation and model pressure time series with significant RMS—often of the same order as the original pressure time series and large enough to obscure deformation signals of at most a few centimeters characteristic of shallow SSEs in other settings, as shown in the differences in the lower panels of Figures 7a–7c.

Frequency spectra of the APG data and model are plotted together in Figures 7d–7e. As with the time series comparisons, the model closely matches the frequency content of the APGs on or near the shelf but does worse for the instruments on the slope and abyssal plain, particularly at frequencies of 0.07 and 0.035 day⁻¹ (periods of 14 and 27 days), where the APG data have larger amplitudes. Across all experiment years, the amplitude at these periods is about twice as large for the APGs than for either of the models, suggesting that the instruments are capturing some oceanographic process that the models do not accurately account for. Instruments off the continental shelf also tend to have elevated amplitudes at higher frequencies when compared to the models, particularly between 0.2 and 0.33 day⁻¹ (periods of 5 and 3 days).

Example pressure time series differences predicted by the WCOFS oceanographic model are shown in Figure 4 (red curve in lower panels) for the same locations as the observations and have a very similar character and RMS as the observed differences. These modeled difference RMS values are given for all of the station pairs in Tables 2 and S1. Differences obtained from model-corrected observations, wherein the model is subtracted from the observation, are plotted in the blue curves of the lower panels of Figure 4, and the difference RMS are also reported in Tables 2 and S1. Applying the model as a correction to the data does not significantly change the RMS of the differences, consistent with the results of Muramoto et al. (2019), who found the variance reduction from subtraction of a barotropic model to generally be less than that achieved through reference station differencing.

The models best predict signals on or near the continental shelf, where R^2 values (equation (1)) of the fit to the pressure time series are as high as 0.6 (Figure 8a). The models have a poorer fit in middle to lower continental slope and abyssal plain locations, with generally negative R^2 values. Despite the better predictability

Table 2
RMS Reduction From Depth Matched Differencing

		Depth	Depth dif.	Separation	Observations		Model		Model corrected obs.	
Year	Station	<i>z</i> (m)	Δz (m)	Δxy (km)	RMS (cm)	Dif. RMS (cm)	RMS (cm)	Dif. RMS (cm)	RMS (cm)	Dif. RMS (cm)
2011–2012	J26A	2,864	--	--	1.5	--	1.3	--	1.6	--
	J34A	2,574	-290	72	1.5	0.6	1.4	0.2	1.8	0.6
	J51A	2,610	-254	244	1.7	0.8	1.4	0.4	1.9	0.8
	J59A	2,371	-493	326	1.8	0.7	1.4	0.5	1.8	0.5
	M06A	1,439	--	--	1.5	--	1.4	--	1.6	--
	J42A	1,540	-101	53	1.5	0.4	1.4	0.2	1.7	0.4
	M03A	1,818	+379	277	1.7	0.5	n/a ^a	n/a ^a	n/a ^a	n/a ^a
	J41A	175	--	--	3.1	--	2.5	--	2.7	--
	FN08A	177	+2	123	2.6	1.7	1.8	1.1	2.3	1.7
	FN14A	173	-2	139	2.7	1.7	1.7	1.2	2.5	1.8
	FN06A	134	--	--	3.1	--	3.0	--	2.2	--
	FN07A	154	+20	8	3.3	0.7	2.5	0.6	2.5	1.0
	J49A	120	-14	59	4.3	1.7	3.5	0.7	2.7	1.5
	FN03A	90	--	--	5.3	--	4.2	--	3.4	--
	FN01A	54	-36	14	6.9	2.5	5.5	1.6	3.3	1.9
	FN19A	75	-15	21	7.1	3.8	4.8	0.8	5.2	3.8
2012–2013	FS20B	2,378	--	--	1.3	--	1.2	--	1.4	--
	G26B	2,357	-21	171	1.3	0.3	1.2	0.3	1.4	0.3
	G34B	2,954	-576	241	1.2	0.5	1.2	0.3	1.4	0.5
	FS16B	1,073	--	--	1.4	--	1.1	--	1.4	--
	FS07B	1,297	+224	23	1.5	0.6	1.1	0.1	1.6	0.6
	M10B	675	--	--	1.5	--	1.3	--	1.4	--
	M18B	720	+45	140	1.8	0.7	1.4	0.3	1.5	0.7
	G09B	842	+167	331	1.5	0.8	1.1	0.5	1.4	0.8
2012–2013	J33B	350	--	--	1.9	--	1.7	--	1.6	--
	J17B	286	-64	146	2.3	0.9	1.8	0.5	1.8	0.9
	G25B	430	+80	354	2.0	1.3	1.5	0.9	1.7	1.4
	FS03B	345	-5	537	1.8	1.3	1.3	1.1	1.5	1.2
	FS08B	120	--	--	3.0	--	1.8	--	2.2	--
	FS11B	132	+12	14	2.7	0.6	1.6	0.5	2.2	0.7
	FS17B	146	+26	27	3.0	0.9	2.1	0.5	2.1	1.1
	G17B	123	+3	106	2.9	0.7	2.4	1.0	1.9	1.1
	FS12B	60	--	--	3.7	--	3.1	--	2.3	--
	FS15B	52	-8	6	5.8	3.6	2.9	0.3	4.5	3.6
	FS19B	87	+27	21	3.9	1.5	2.1	1.5	2.9	2.3
2014–2015	MJ01A	2,908	--	--	1.4	--	2.7	--	2.6	--
	O2	1,909	-999	12	1.6	0.8	2.4	0.8	2.5	1.2
	LJ01B	775	--	--	1.6	--	1.9^b	--	2.0^b	--
	M15D	933	+158	263	1.7	1.0	1.8 ^b	0.4 ^b	2.1 ^b	1.0 ^b
	J09D	252	--	--	3.0	--	1.8	--	2.9	--
	J17D	285	+32	71	2.8	1.1	1.8	0.4	2.6	1.1
	FS11D	150	--	--	3.2	--	2.2^b	--	3.1^b	--
	FS17D	145	-5	15	2.9	1.1	2.9 ^b	1.1 ^b	2.7 ^b	1.7 ^b
	J25D	136	-14	448	3.6	2.0	3.6 ^b	2.1 ^b	4.1 ^b	2.6 ^b
	FS42D	95	--	--	3.5	--	3.3^b	--	3.3^b	--
	FS12D	55	-40	30	4.2	1.2	6 ^b	0.8 ^b	4.1 ^b	1.2 ^b

Note. We include here only differences for which depths are reasonably well matched: within tens of meters for instruments on or near the continental shelf, within hundreds of meters for instruments on the middle to lower slope, and within ~1,000m for instruments on the abyssal plain. The first station in each group, indicated in boldface, acts as the reference, against which all others were differenced. Gray and white shading are used to visually separate station groups. We report the depth of each instrument ("Depth"), the depth difference relative to the reference station ("Depth dif."), the lateral distance from the reference station ("Separation"), and the RMS of each pressure time series and difference ("Observations"). RMS values from the WCOFS model at the same locations are also included ("Model"), as are those obtained by applying the model as a correction to the data prior to differencing ("Model corrected obs."). In the 2014–2015 year, the LiveOcean model is used for those instruments within its domain, while the remainder use a truncated WCOFS model (which ends in December 2014). *z*: depth; Δxy : horizontal separation; RMS: RMS of pressure time series; Dif. RMS: RMS of difference time series.

Abbreviation: n/a: not available; RMS: root-mean-square; WCOFS: West Coast Ocean Forecast System.

^aModel unavailable for station M03A. ^bWCOFS model available only until 31 December 2014.

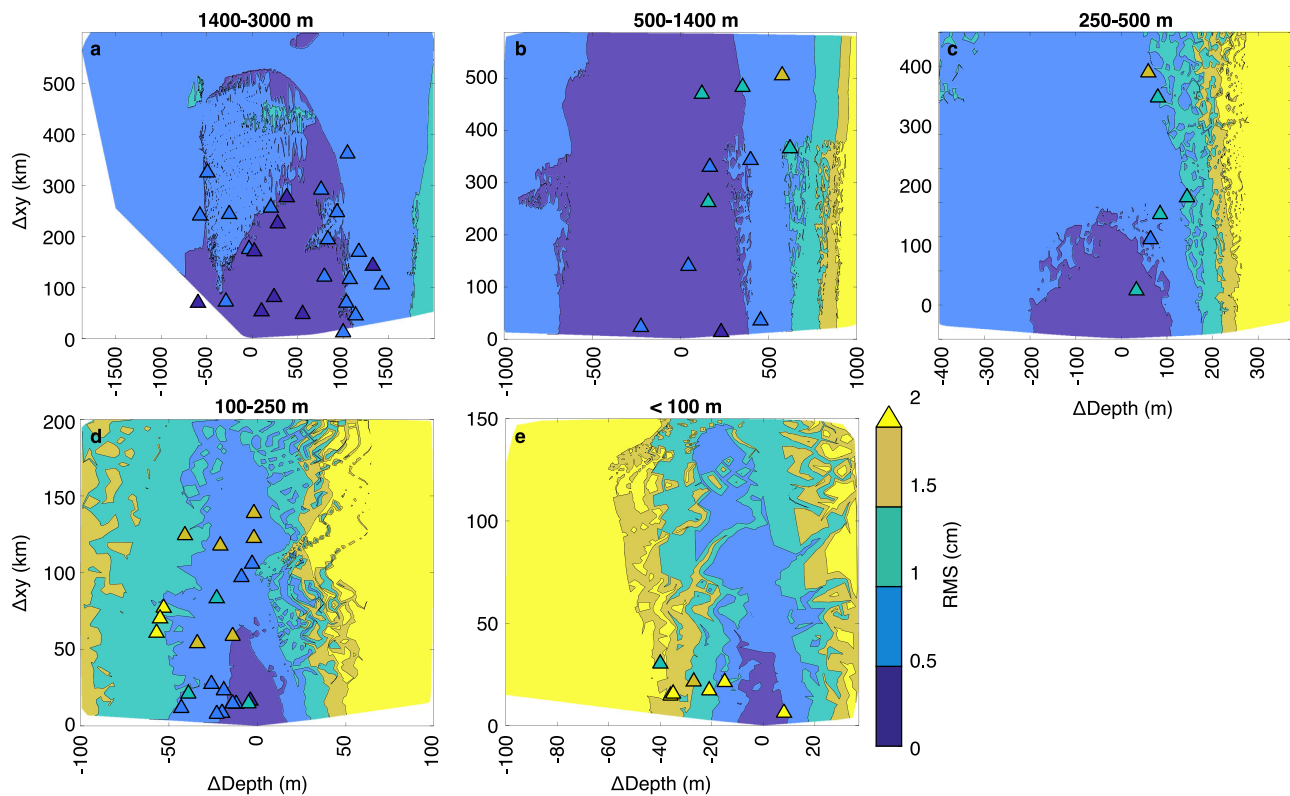


Figure 5. Pressure difference root mean square (RMS) versus lateral separation and depth difference. Triangles represent observed differences from the absolute pressure gauge (APG) data, color coded by RMS. Contours show predictions from the West Coast Ocean Forecast System (WCOFS) oceanographic model, using the same color scale but faded for display purposes. (a) Instruments between 1,400- and 3,000-m depth and model reference location at 2,581 m. (b) Instruments between 500- and 1,400-m depth and model reference location at 1,103 m. (c) Instruments between 250- and 500-m depth and model reference location at 394 m. Note that one difference at large separation is excluded from the APG data for display purposes. (d) Instruments between 100- and 250-m depth and model reference location at 121 m. Note that two differences at large separation are excluded from the APG data for display purposes. (e) Instruments less than 100-m depth and model reference location at 57 m. The model reference locations are shown by open symbols in Figure 6a. We use the convention that ΔDepth is positive when the reference location is deeper than the location from which it is subtracted and negative when it is shallower. For the APG data, the reference station is chosen to be that which is most similar to the model reference for that depth bin, for consistency in our sign convention.

at shallow locations, those locations are left with larger RMS than the more poorly predicted deep locations (Figure 8b) when model-corrected because of the significantly larger amplitudes of pressure signals in shallow water.

The circulation models capture a significant portion of localized oceanographic processes and may therefore be used to better understand those processes. We assessed the signal similarity between locations, and thereby the effectiveness of differencing, by selecting grid points within the model domains and differencing their predicted pressure time series against those of all other grid points in the domain, then calculating the RMS of the differenced signals. Results of this analysis are shown in Figures 6b–6d, where difference RMSs are contoured for reference locations on the abyssal plain, continental slope, and continental shelf in the WCOFS model. The oceanographic models suggest broadly similar oceanographic characteristics along isobaths, within 0.5-cm RMS over hundreds of kilometers, while RMS changes rapidly across isobaths, as seen most clearly on the upper slope and shelf. These characteristics of the oceanographic models mirror those seen in the APG dataset, suggesting that the models accurately predict the regionality of seafloor pressure signals and their comparability between locations. To directly compare APG observations and model output, we contour modeled difference RMS against depth difference and separation for a sample location within each of the depth bins in Figure 5. This shows that the model predicts that lower RMS values are achievable over greater separations and depth differences than seen in the observations, which is unsurprising given that the model underpredicts signal amplitudes and is missing certain spectral content.

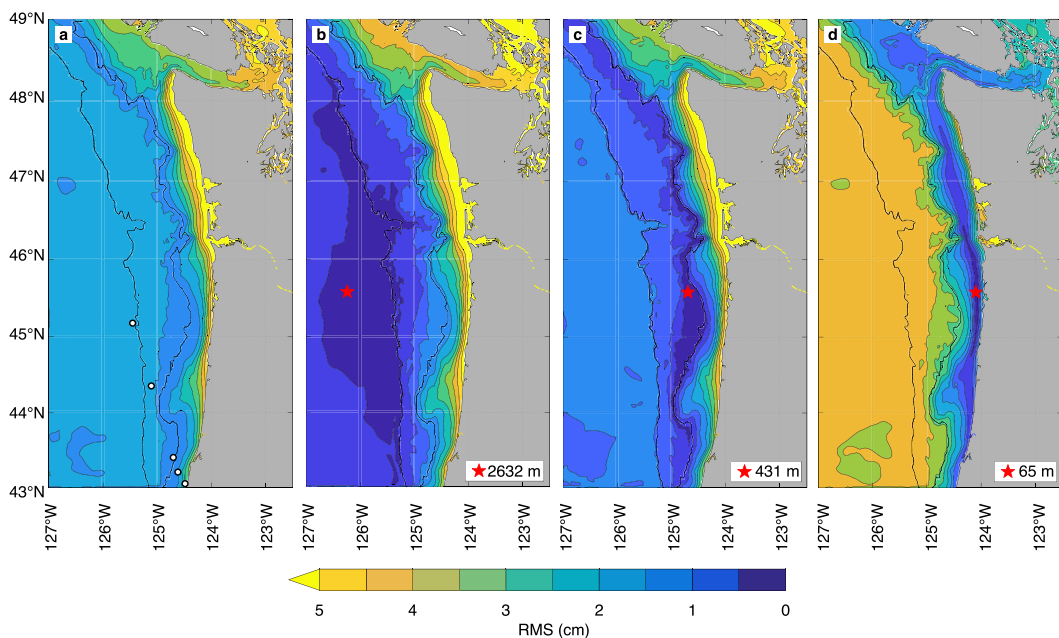


Figure 6. (a) Contours of modeled bottom pressure root mean square (RMS) from 2013 to 2014 of the LiveOcean model, with a Godin 24-24-25 filter (Godin, 1972) applied and a third-order polynomial fit removed. The open circles indicate the model locations used in Figure 5. (b–d) Contours of RMS of modeled differences relative to the starred reference locations for all grid points in the model, with depth indicated in legend, for an abyssal plain, continental slope, and continental shelf location, respectively. The black contours show 300- and 2,000-m isobaths.

3.3. SSE Deformation Modeling

Our base model emulates the characteristics of shallow SSEs from Hikurangi and the Japan Trench. The parameters for this model and the variations we explore are presented in Table 1. The Mw 6.4, $\Delta\sigma_E = 0.057$ -MPa base model (Figures 3 and 9a), with 32-cm peak slip centered 72 km offshore from the coastline at 8-km depth below the seafloor, results in two lobes of vertical seafloor deformation: a trenchward zone of up to 5.5-cm uplift and a landward zone of up to 4.1-cm subsidence, with a total area of deformation greater than ± 1.5 cm of approximately $4,000 \text{ km}^2$. This two-lobed deformation pattern is found in all our models, with the subsidence lobe consistently smaller in both area and amplitude. As a whole, the region of deformation scales with the dimensions of the slip patch; deformation does not extend much beyond the along-strike limits of slip, but the combined deformational area does extend tens of kilometers beyond the updip and downdip extent of slip.

We assessed the detectability of our models by generating two idealized lines of stations, with pressure time series extracted from the LiveOcean model, from which to detect the SSE: one running roughly perpendicular to strike with 10-km spacing and the other running roughly parallel to strike along a contour of constant depth with 12-km spacing (Figure 9a). The modeled deformation at each station location was added linearly to that station's modeled pressure over the event duration of 14 days. Both lines pass through the point of maximum uplift, and each station was differenced against a reference station at the end of its respective line. In the case of the depth-matched station line, the reference location was sometimes moved from one end of the line to the other to avoid overlapping the deformation region. In the differences, uplift results in a decrease in pressure and is expressed as a negative offset, while subsidence is expressed as a positive offset. For both lines, the uplift signal is clearly visible above the noise in the difference time series (Figures 9b and 9c). This is especially true for the depth-matched station line, for which oceanographic noise has been largely eliminated. Subsidence signals are more difficult to detect in the strike-perpendicular line, as they occur high on the continental slope and on the shelf, where oceanographic noise is high and dissimilar to that of the reference station on the abyssal plain. Changing the onset time of slip to coincide with an oceanographic signal of opposite sign (Figure S5) obscures deformation in the strike-perpendicular line for all but one record and illustrates the utility of depth-matched differencing. Extending the duration of slip to 30 days (Figure S6) makes deformation more closely resemble an oceanographic signal and is more susceptible to partial

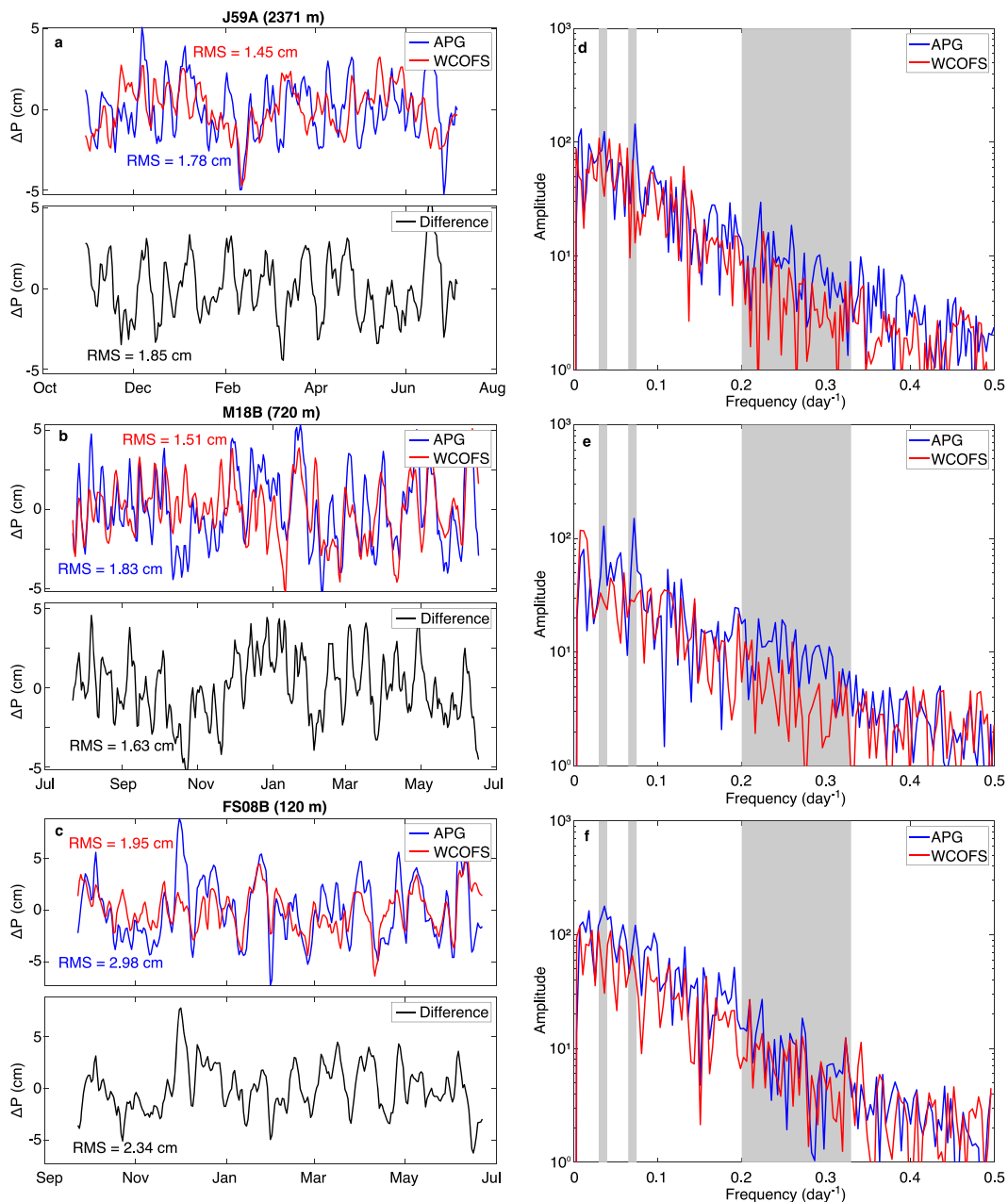


Figure 7. Comparison of absolute pressure gauge (APG) data and modeled bottom pressure for the 2012–2013 year at select locations. (a–c) Pressure time series (top panel) and differences (bottom panel) for the data and West Coast Ocean Forecast System (WCOFS) model for continental shelf, slope, and abyssal plain locations. (d–f) Amplitude spectra of the time series at the same locations. Grayed areas indicate frequencies of 0.07, 0.035, and 0.2–0.33 day^{-1} , where APG amplitudes are consistently larger than predicted by the model.

removal by a polynomial correction, again illustrating the importance of the noise-reduction obtained by our method.

Figure 10a shows the modeled deformation that results from an event of the same magnitude and stress drop as the base SSE, shifted up-dip so as to occur adjacent to the trench, with 28-cm peak slip centered 100 km offshore at 5-km depth below the seafloor. This shift results in both deformation lobes similarly shifting to deeper waters, which provides a more uniform oceanographic setting for the uplift lobe, which is easily identified on difference plots for either station line (Figures 10b and 10c). Much of the subsidence lobe, including the site of peak negative deformation, is still on the middle to upper slope and so these signals are not readily

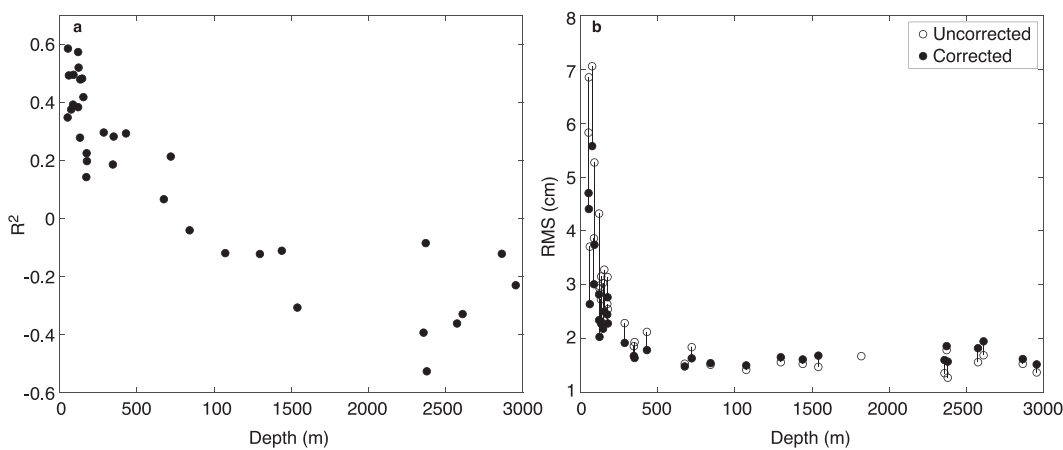


Figure 8. (a) R^2 of the fit of the 2011–2013 West Coast Ocean Forecast System (WCOFS) modeled bottom pressure to the observed absolute pressure gauge data as a function of instrument depth. A positive R^2 signifies that variance is reduced by differencing, while a negative R^2 signifies that variance is increased. (b) Comparison of root mean square versus depth of absolute pressure gauge pressure time series before (open circles) and after (filled circles) correcting with the WCOFS model, as a function of instrument depth.

distinguished in the strike-perpendicular line, given the significant residual noise in the differences. Moving slip downdip, with 31-cm peak slip centered 58 km offshore at 10-km depth below the seafloor (Figure S7), shifts deformation into shallower waters, in which larger oceanographic signals obscure deformation on the strike-perpendicular line for both uplift and subsidence lobes. In both the updip and downdip scenarios, deformation is clearly identifiable on the depth-matched line.

Another model variation held the magnitude of the SSE constant and reduced the stress drop to $\Delta\sigma_E = 0.014$ MPa (Figure 11a). This corresponds to $\Delta\sigma_M = 0.010$ MPa, the lower limit of stress drop scaling for SSEs reported by Gao et al. (2012). We accomplished this by increasing the along-strike halfwidth of our Gaussian from 19 to 58 km, holding the updip and downdip extent of the fault patch constant, and decreasing the peak slip to 11 cm. The resulting deformational pattern is elongated along-strike, with decreased amplitudes in both positive and negative lobes and a significant region of nondetectable deformation between lobes. The area of uplift >1.5 cm is approximately $1,400 \text{ km}^2$, while the area of subsidence >1.5 cm is approximately 350 km^2 . For the strike-perpendicular differences (Figure 11b), this deformation is too small to be distinguished from the oceanographic noise. For the depth-matched differences (Figure 11c), on the other hand, the signal is larger than the residual noise and is captured on a large number of stations, which would lend confidence that it is a real geophysical signal. We also increased the stress drop of the base model to $\Delta\sigma_E = 0.22$ MPa (Figure S8), or $\Delta\sigma_M = 0.10$ MPa, the upper stress drop limit of Gao et al. (2012), by decreasing the along-strike halfwidth to 7.3 km and increasing the peak slip to 82 cm. This results in larger-amplitude deformation lobes, but with areas slightly smaller than those of the base model, with approximately $3,000 \text{ km}^2$ of deformation greater than ± 1.5 cm.

A low-magnitude model was also explored (Figure 12a) with $M_w 5.9$ and $\Delta\sigma_E = 0.022$ MPa by decreasing the along-strike halfwidth of our slip Gaussian to 17 km and the maximum slip to 9 cm. This leads to a very small area of deformation on the seafloor, approximately 1 km^2 of >1.5 -cm uplift and no subsidence >1.5 cm. The deformation is indistinguishable from oceanographic noise on the strike-perpendicular station line (Figure 12b) and is visible on only one station in the depth-matched line (Figure 12c) and thus, near the detection limit of our method. Another variation increased the magnitude to $M_w 6.9$ and $\Delta\sigma_E = 0.022$ MPa (Figure S9), near the upper limit of what has been observed in Cascadia deep SSEs (e.g., Hall et al., 2018), by increasing the along-strike halfwidth to 60 km and increasing the peak slip to 65 cm. This model has significantly increased area and amplitude of deformation greater than ± 1.5 cm relative to the base model. Regardless, the strike-perpendicular line is still unable to clearly resolve the subsidence signal on and near the continental shelf.

The stress drop range given by Gao et al. (2012) is derived from observations of deep SSEs in Cascadia, and it is possible that shallow SSEs may have stress drops lower than $\Delta\sigma_M = 0.01$ MPa, as suggested by the small

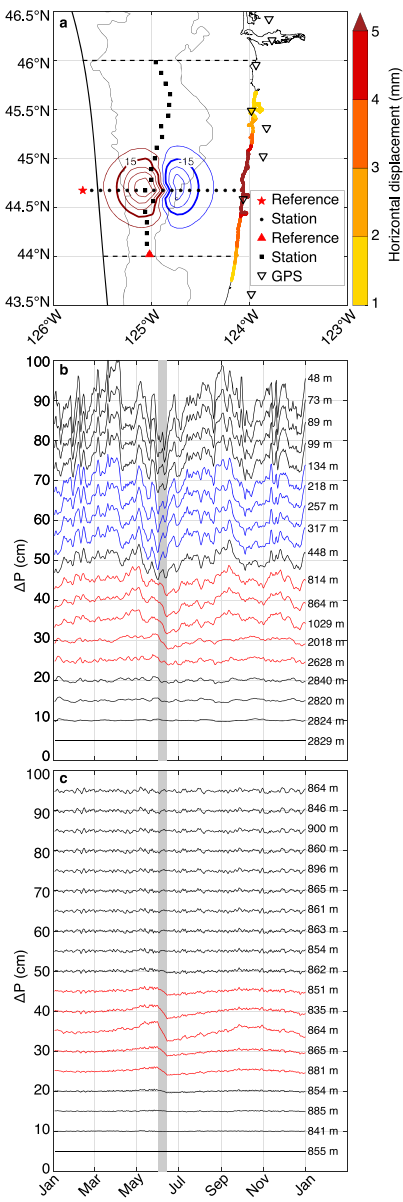


Figure 9. Synthetic slow-slip earthquake modeling results for our base model, a midslope M_w 6.4 event of 2-week duration, beginning on 1 June 2013. (a) Contours of seafloor deformation beginning at 5 mm with an interval of 10 mm on a regional map, overlain with modeled stations (squares and circles) running through the site of peak deformation and reference locations for subsequent differencing plots. The bold contours indicate vertical deformation of ± 15 mm. Instrument spacing is 12 km along isobaths and 10 km across isobaths. Coastal and near-coast Global Positioning System (GPS) instrument locations are labeled as inverted triangles and modeled horizontal deformation is color coded at the coastline. The bold black lines show the trench and coastline, the thin black lines show 300- and 2,000-m isobaths, and the partially locked Oregon region is demarcated by the dashed lines. (b) Time series plots of modeled seafloor pressure differences of the strike-perpendicular station locations, relative to the red star location in (a). Differences from the stations overlying the uplift lobe (> 15 mm) are displayed in red while those overlying the subsidence lobe (< -15 mm) are displayed in blue. (c) Time series as in (b) but for the depth-matched stations and red triangle reference location. Time series are offset for display purposes and station depths are indicated next to each.

amount of slip reported in the events of Araki et al. (2017). To this end, we model a near-trench M_w 6.2 SSE with maximum 4-cm slip and a stress drop of $\Delta\sigma_E = 0.006$ MPa ($\Delta\sigma_M = 0.005$ MPa; Figure S10a). Such an event produces no vertical deformation greater than 1.5 cm. Both station lines are effectively depth-matched over the small deformation area produced by this event, and in both sets of differences (Figures S10b and S10c) the uplift signal is of the same amplitude as the residual noise. Given that the synthetic time series come from the LiveOcean model, which does not contain the full complexity of the observational data (Figure 7), and that the deformation signal is comparable with the noise floor, this event is clearly below the detection limit of our method.

4. Discussion

4.1. Detection of Slow-Slip Events in Observational Data

In order to be confidently detected in the available APG data, a shallow SSE would need to (1) be concurrent and collocated with the sensor network, (2) be of sufficient geographic extent to cause deformation at more than one station, and (3) produce sufficient vertical seafloor displacement to be resolvable above the residual noise in the APG differences. Ideally, sensors would resolve both the trenchward uplift and shoreward subsidence signals, as their relative positions are diagnostic.

Under these qualifications, we found no evidence of a shallow SSE in the 4 years of our dataset. To our knowledge, there are no published reports of related activity recorded on CI seismometers or land-based instruments during this interval. While it is possible, perhaps likely, that no SSE comparable to those seen at Hikurangi and the Japan Trench occurred during the study period, we infer that the pressure data used in the study were insufficient to confidently identify such a SSE, should it have taken place. The CI APG network was not designed with the intention of measuring SSE deformation. Stations were clustered offshore Washington and California, where the subduction zone may not be slipping, according to current models of plate locking (Burgette et al., 2009; Schmalzle et al., 2014). Outside of these clusters, instruments were broadly spaced, and the deformation produced in any of our SSE modeling scenarios would not likely cover multiple instruments. Instruments also shifted between northern and southern domains between experiment years, so only about half of the margin was instrumented at any given time. Additionally, the sensitivity of the differencing method depends upon the availability of depth-matched stations for differencing, which were not consistently available. As shown in Figure 5 and Table 2, instruments below 1,400-m depth can be effectively differenced to ≤ 1 -cm RMS even in the absence of a closely depth-matched pair, but such instruments represent only some 35% of all instruments and have limited spatial coverage outside of the 2011–2012 year, while instruments shallower than 250 m require depth matching to avoid RMS as high as 5 cm. The OOI and Oregon benchmark instruments used to supplement these data help increase coverage near Oregon but overlap in time with the CI data for only 1 year of the experiment.

Some oceanographic bottom pressure signals have timescales and amplitudes similar to those of SSE deformation. Such signals, if not properly corrected, have the potential to be misidentified as geophysical deformation. This is explored in Figure 13, for which the standard differencing

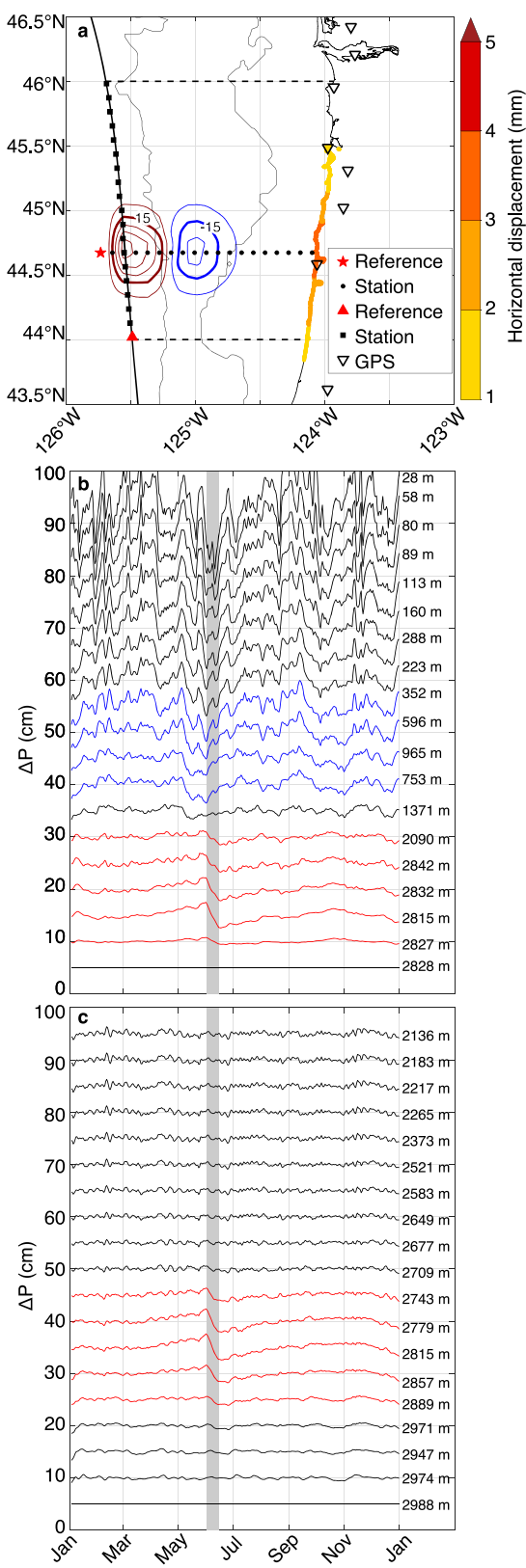


Figure 10. As in Figure 9 but for a trench-adjacent slow-slip earthquake. Note that deformation occurs on the incoming plate due to the 3 km of sediment cover above the updip terminus of our modeled plate interface.

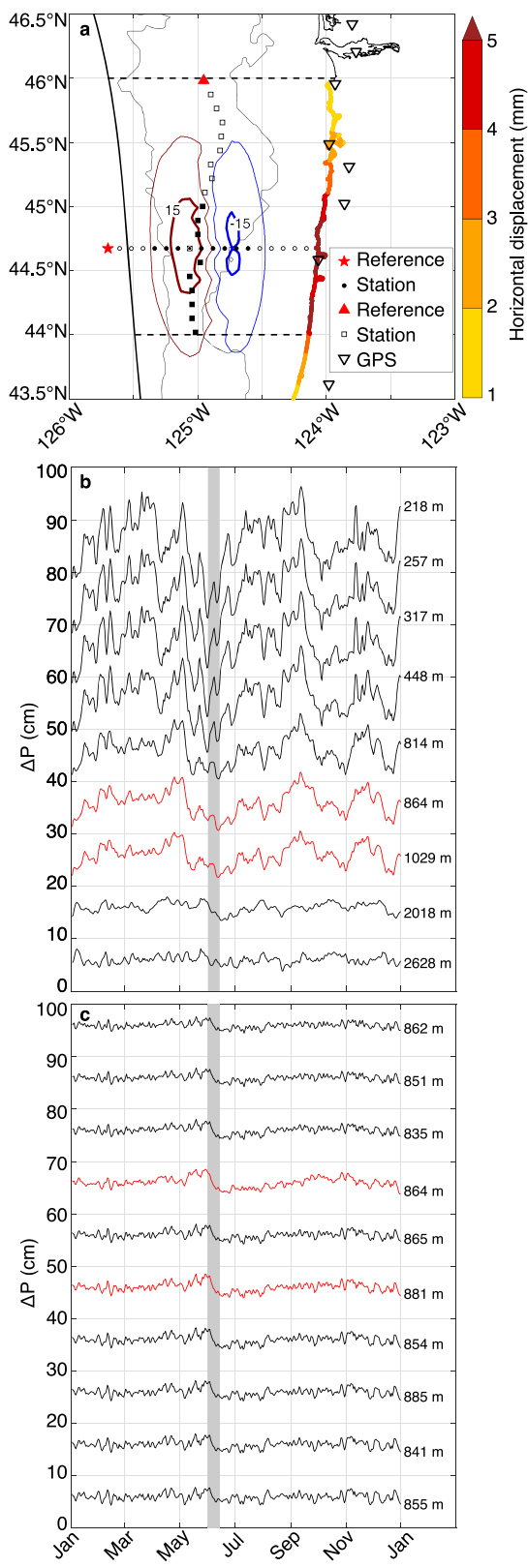


Figure 11. As in Figure 9 but for a slow-slip earthquake with a stress drop of $\Delta\sigma_E = 0.014$ MPa. Infilled station markers in (a) are those for which modeled pressure differences are shown in (b) and (c).

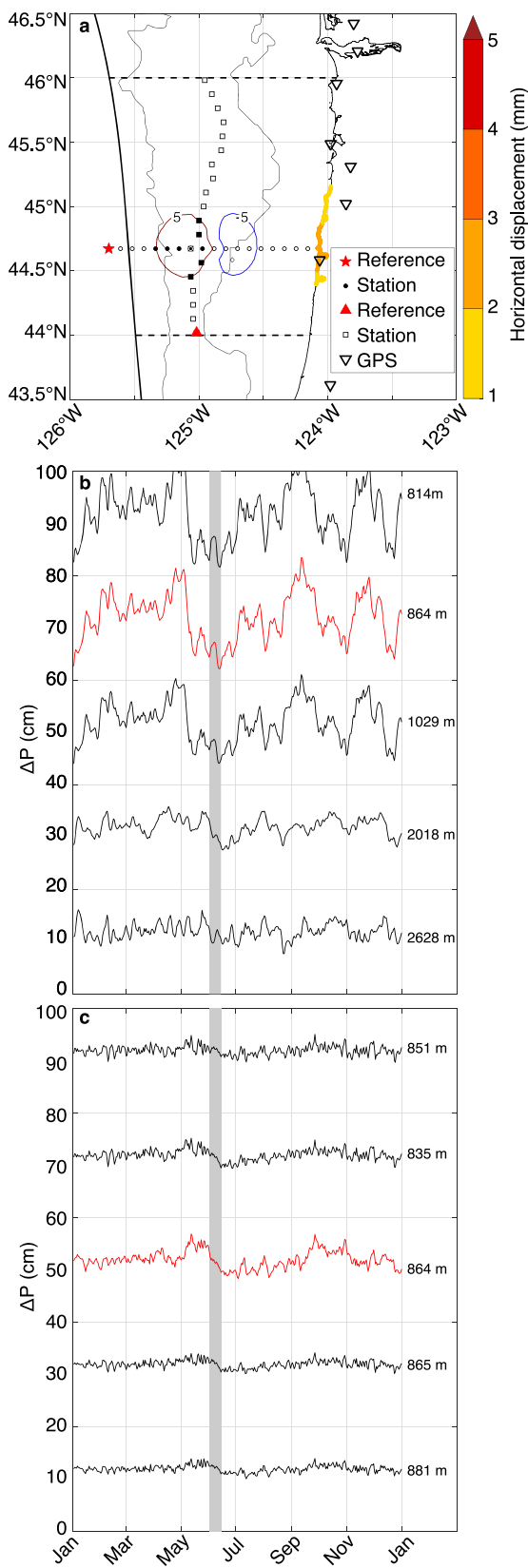


Figure 12. As in Figure 9 but for a Mw 5.9 slow-slip earthquake. Infilled station markers in (a) are those for which modeled pressure differences are shown in (b) and (c).

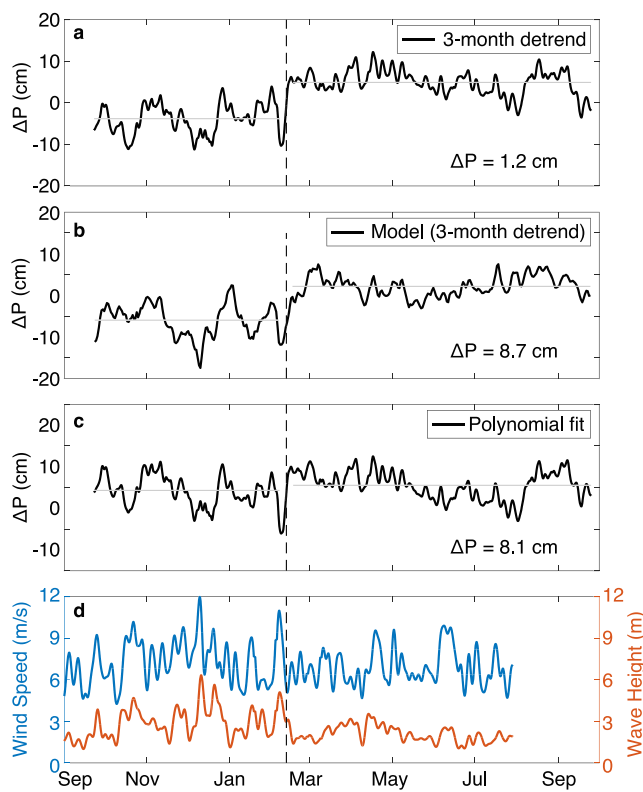


Figure 13. Example of the standard differencing technique producing a significant false slow-slip earthquake detection between instruments J25D and MJ01A from the 2014–2015 year (locations shown in Figure 2c). The dashed vertical line indicates the perceived onset time of the SSE. The horizontal gray lines mark the average pressure before and after the event, with the difference between these given in the bottom right of each figure. (a) The difference time series using polynomial-corrected pressure records. (b) The difference time series from applying a polynomial correction to the reference station and detrending the second station using the linear fit to only the three months of data preceding the presumed SSE (Wallace et al., 2016). (c) Recreation of (b) using the LiveOcean model in place of absolute pressure gauge records. (d) Hindcast wind speed and wave height from National Oceanic and Atmospheric Administration (NOAA) Wavewatch III (Tolman, 2009) during the same time interval, low-pass filtered (0.2 day^{-1} cutoff) to emphasize long-period signals.

technique using a reference instrument on the incoming plate (e.g., Wallace et al., 2016) is applied to a pressure record from 2014 to 2015 in Cascadia that has previously been speculated to have recorded a SSE transient signal (Bletry et al., 2017). A near-trench reference pressure record at 2,908-m depth, presumed to have experienced little or no deformation, is fit with a third-order polynomial to remove instrument drift and act as the regional oceanographic correction. A pressure record from the upper plate, 62 km away at 136-m depth, presumed to have undergone deformation during a specific time, is detrended using 3 months of data prior to the event, meant to represent the linear component of the sensor drift. The two pressure records are then differenced (Figure 13a), and the offset due to deformation is determined by calculating the mean pressure before and after the event. This processing method produces an offset well above the noise. However, applying the same method to predicted pressures from the same locations in the LiveOcean model (Figure 13b), which contains no deformation signal, results in a comparable perceived offset. Conversely, when no assumptions are made about event timing and the same two instruments are both corrected with polynomials then differenced (Figure 13c), the offset between the same time intervals is well below the residual noise. Comparing the pressure time series to wind and wave hindcasts from NOAA's Wavewatch III (Tolman, 2009) reveals a significant change in these surface observables concurrent with the perceived SSE (Figure 13d), suggesting that storm events can generate seafloor pressure signals that may easily be mistaken for geophysical deformation due to their similar amplitude and duration. Further, these storm signals can be seen over large areas and across multiple sensors, with varying amplitudes, again resembling qualities of a SSE. However, Figure 13 also shows that

these storm signals are present in the oceanographic models and in observations of sea surface conditions, so by examining these data false detection of SSEs can be minimized.

4.2. Oceanographic Signal Reduction in Seafloor Pressure Data

Although the oceanographic circulation models reproduce much of the fluctuations in observed seafloor pressure time series, they are not sufficiently accurate at this time to act as a correction for oceanographic signals on observational data, consistent with the results of Muramoto et al. (2019). The largest disagreement occurs at periods of 14 and 27 days, which closely match the spring-neap tidal cycle and the anomalistic month, the period over which the moon goes from apogee to apogee. Both cycles modulate tidal amplitudes at these periods, possibly in part in the form of internal tides generated outside of the model domains and not included in the boundary conditions. Comparisons of model and APG time series also show that pressures at deep locations are not predicted as well as pressures at shallow locations, particularly at periods of 3 to 5 days (Figure 7). This is not surprising, as the majority of the observations through which these models are validated are located on the continental shelf (Giddings et al., 2014; Kurapov et al., 2017) and shelf physics are more deterministic due to the heavy influence of sea surface forcings and bottom boundary dampening. At depth, unstable processes like mesoscale eddies and cuddies (California Undercurrent eddies) are proportionally larger contributors to circulation and energy transfer (e.g., Collins et al., 2004), making pressure inherently less predictable on the slope and abyssal plain. Given that these oceanographic models were not designed for calculating seafloor pressures, further studies are needed to understand how models could be optimized for this purpose, such as by accurately determining the physical properties of near-bottom waters and using available seafloor pressure data for validation.

Despite the differences between model and observation, amplitude and frequency characteristics are sufficiently similar to be used for studying the propagation and comparability of seafloor pressure between locations. The oceanographic models suggest that seafloor pressure differences with $\leq 1\text{-cm RMS}$ can be achieved between locations at the same depth separated by hundreds of kilometers, as demonstrated in Figures 5 and 6. The continuity in oceanographic seafloor pressure at constant depth is consistent with patterns identified by Hughes et al. (2018), who found seafloor pressure to closely reflect basin-scale circulation processes while being largely unaffected by mesoscale eddy effects that typically have significant impact on physical oceanographic observables. They additionally suggest that measurements of ocean bottom pressure, along with observations of bottom density and currents, could lead to improvements in models of global oceanographic processes. Such improvements could in turn improve the comparability between modeled and observed pressures as these models become closer approximations to the real ocean system.

Differencing of depth-matched instruments is highly effective at reducing the nontidal oceanographic component of bottom pressure time series for any instrument depth. The degree to which low RMS can be maintained over increasing separation is a function of the depths of the stations being compared, as seen in Figure 5 and Tables 2 and S1, where the shallowest stations require the most similar depths. All of the 25 differences for instruments at depths greater than 1,400 m (Figure 5a) have $\text{RMS} < 1\text{ cm}$, with a mean of 0.6 cm, at separations as large as 360 km and up to 1,400-m depth difference. For instruments at 1,400 m $>$ depth $>$ 500 m (Figure 5b), the differences restricted to a depth difference less than 456 m and separation less than 344 km have a mean RMS of 0.7 cm, with 6 of 7 having $\text{RMS} < 1\text{ cm}$. The mean depth difference for these restricted differences is 240 m, and the mean separation is 164 km. For instruments at 500 m $>$ depth $>$ 250 m (Figure 5c), there are very few data points to draw from, with five of the seven total differences coming from instruments separated by more than 150 km (Figure 5c). Of the remaining two differences, one at a depth difference of 64 m and separation of 146 km has an RMS of 0.9 cm, while the other at a depth difference of 33 m and a separation of 71 km has an RMS of 1.1 cm. For instruments at 250 m $>$ depth $>$ 100 m (Figure 5d), the differences restricted to a depth difference less than 44 m and separation less than 106 km have a mean RMS of 1.0 cm, with 10 of 15 having $\text{RMS} < 1\text{ cm}$. The mean depth difference for these restricted differences is 19 m, and the mean separation is 37 km. At instrument depth $< 100\text{ m}$, no differences yield $\text{RMS} \leq 1\text{ cm}$ (Figure 5e). Thus, Cascadia APG data provide evidence that at depths $> 100\text{-m}$ distal locations at comparable depths experience highly similar pressure fluctuations and suggest that effective differencing under our method does not act as a significant constraint on distance between instruments for a deployment.

Given the above relationships, we suggest the following restrictions on depth difference and separation to enable effective differencing to better than 1-cm RMS. Instruments at 250 m $>$ depth $>$ 100 m should be

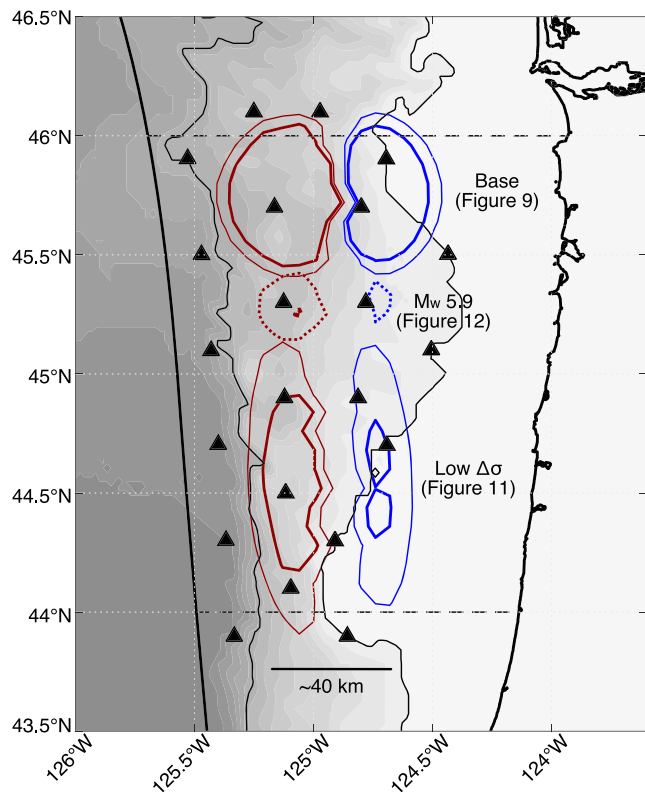


Figure 14. A possible configuration for an idealized absolute pressure gauge network for detecting shallow slow-slip earthquakes offshore central Oregon. The bold black curves show the coastline and trench as per McCrory et al. (2012), the fine lines show 300- and 2,000-m isobaths, and the dashed horizontal lines demarcate the extent of the partially locked zone (Burgette et al., 2009; Schmalzle et al., 2014). The triangles indicate our recommended station locations. The vertical deformation from the base model (Figure 9) is shown by the solid ellipsoids in the north, the low-stress variation (Figure 11) is shown by the solid ellipsoids in the south, and the low M_w variation (Figure 12) is shown by the dashed ellipsoids. All have been offset from their modeled locations for display purposes. Thin ellipsoids contour 1-cm deformation, while bold ellipsoids contour 1.5-cm deformation, with red indicating uplift and blue indicating subsidence. Note that the low M_w model produces only a small region of 1.5-cm uplift and no region of 1.5-cm subsidence.

lower stress drop SSE produces smaller amplitude deformation and requires more sensitive observation, while a higher stress drop SSE has a smaller footprint and requires a denser network.

The base SSE model (Figure 9) produces absolute deformation greater than 1.5 cm of differential signal (combined uplift and subsidence lobes) in an approximate ellipsoid with a 65 km N-S axis and 66 km E-W axis, though there is a narrow, ~6 km, region between uplift and subsidence where nonresolvable deformation occurs. For such dimensions, instrument spacing of approximately 30 km is sufficient to ensure the identification of a significant deformation signal on more than one instrument. This spacing would serve as a bare minimum for detection but would not provide sufficient data points for a detailed slip inversion.

For the purpose of detecting a SSE off central Oregon comparable to our base model, we recommend 22 instruments in four depth-matched sets (Figure 14), which together ensure a resolvable signal on multiple instruments. Our geometry has six instruments just landward of the trench at 2,000–3,000 m, seven on the lower slope at 1,100–1,600 m, three on the upper slope at 450–700 m, and six below the shelf break at 300 m. The shelf-break locations were selected to have precisely matched depths (readily achievable with current ship-based technologies), while the trench-adjacent stations, which require less restrictive depth

depth matched to within ~10 m and separated by less than ~100 km. There are limited data from instruments at 500 m > depth > 250 m, so conservatively, these should also be depth matched to within ~10 m and separated by less than ~100 km. Instruments at 1,400 m > depth > 500 m should be depth matched to within ~200 m and separated by less than ~200 km. Instruments deeper than 1,400 m can differ in depth by ~1,000 m and separated by ~300 km.

4.3. Idealized Sensor Geometry for Slow-Slip Detection Off Oregon

The above difference relationships show that the standard differencing technique, which uses a reference station, or stations, on the incoming plate is effective at removing oceanographic noise only for other stations on the abyssal plain and lower continental slope. Moving up the slope and onto the shelf, the oceanographic signals vary too much between locations for differencing with an abyssal plain station to provide an accurate correction. This complication can be overcome by designing networks of depth-matched instruments over a range of depths so that all pressure data are paired with a suitable reference for correction. For such a network, we prescribe a 1.5-cm threshold for the unambiguous detection of deformation signals, based on the 49 depth- and range-restricted differences discussed above. For these data, a threshold of 1.5 cm represents >1.5 times the standard deviation for 86% of our depth- and separation-restricted differences. For 57% of these differences (predominantly instruments deeper than 500 m) this threshold is > 2 times the standard deviation, so our detection threshold for this network likely represents a conservative overestimation.

The region of Cascadia offshore central Oregon is a good location to search for shallow SSEs in Cascadia because the coupling offshore is inferred to be lower than for the rest of the subduction zone (Burgette et al., 2009; Schmalzle et al., 2014). For this reason, we use our geophysical modeling results to recommend an optimized station configuration for the detection of SSEs in this region. The geometry of any deployment is dependent upon the size of event that needs to be measured; smaller SSEs should occur frequently but produce less deformation, while larger SSEs will produce more deformation but occur less often. Additionally, for a given moment release,

matching, were instead chosen to parallel the trench of McCrory et al. (2012). The intermediate lines were similarly allowed to vary in depth, within the limits described in this work, and were selected to evenly fill the distance between the shallow and deep lines. Each set of instruments has 44 km N-S spacing, but the lines are staggered to minimize the gaps that would result from a regular grid. In Cascadia the distance between shelf break and trench varies with latitude, resulting in nearest-neighbor station spacing as small as 17.5 km and as large as 31 km, dense enough to pick up multiple resolvable signals, regardless of where the SSE should occur. The density of this recommended network also increases the likelihood of capturing the diagnostic relative positioning of uplift and subsidence. Such a geometry would also ensure that multiple instruments record resolvable deformation from a larger magnitude SSE (e.g., Figure S9) as well as for a high stress drop event, for which the area of deformation does not decrease significantly relative to the base model (e.g., Figure S8). To resolve deformation on multiple instruments during a low stress drop SSE (Figure 11), a denser E-W network would be required, on the order of 15-km spacing. This is because the areas of deformation greater than ± 1.5 cm in the low stress drop model are significantly narrower, particularly the subsidence lobe, and there is an ~ 20 -km region of nonresolvable deformation between uplift and subsidence lobes, resulting in a much narrower footprint overall for this event.

We view the network described here as the sparsest array that ensures resolvable deformation signals on multiple instruments for SSEs of $M_w \geq 6.4$. Denser networks would allow for better characterization of the slip, at the cost of either a smaller instrumented area or the need for more instruments. However, the $\Delta\sigma_E = 0.014$ MPa (Figure 11) and $M_w 5.9$ (Figure 12) models suggest that increased density will not significantly aid the detection of lower-magnitude or lower-stress drop SSEs, as events smaller than these do not produce significant regions of ± 1.5 -cm vertical deformation (e.g., Figure S10). This scenario is demonstrative of the importance of further exploring the effectiveness of depth-matched differencing. If oceanographic noise can be reduced to allow a lower detection threshold of 1 cm, the area of resolvable deformation increases drastically, as shown in Figure 14. The oceanographic models, though they tend to underpredict signal amplitudes, suggest that difference RMS less than 0.5 cm can be achieved throughout the margin with sufficiently well-matched depths and the station spacing recommended here (Figure 5). Similarly, the APG differences reported in Tables 2 and S1 include a few difference RMS values ≤ 0.5 cm, though there are limited similar-depth, closely spaced instruments from which to draw conclusions.

A sufficiently large offshore SSE, or one occurring sufficiently far downdip, will produce deformation resolvable on land-based GPS stations. GPS records of deep SSEs in Cascadia show that horizontal displacements of only a few millimeter are readily resolved at a single station (e.g., Rogers & Dragert, 2003; Szeliga et al., 2008), but these offsets are meaningfully interpreted only with concurrent signals on multiple instruments. The detectability of offshore slow slip on land-based systems is also inhibited by the increased noise levels and prevalence of anomalous signals at coastal GPS stations, effects infrequently discussed in the literature, particularly on horizontal components. However, Tian (2011) identifies anomalous horizontal signals in the Crustal Motion Observation Network of China and points to complex oceanic loading at coastal sites. Similarly, Nordman et al. (2015) generate models of nontidal loading to explain anomalous horizontal signals on instruments bordering the Baltic Sea, on the order of a few mm, consistent with displacements calculated by Geng et al. (2012) for instruments bordering the North Sea during a large storm surge. Thus, we assume a detection threshold for horizontal displacement on a single coastal instrument to be $\sim 4\text{--}5$ mm, though even a large signal would be inherently uncertain if not corroborated by a concurrent measurement. There is also the issue of instrument density relative to expected coastal deformational areas, with spacing between coastal instruments ranging from 20 to 130 km (<https://www.unavco.org/instrumentation/networks/map/map.html>). Horizontal displacements decay rapidly inland, reaching near-zero values within <50 km, so only those instruments nearest the coastline would be expected to record resolvable deformation. Current interest in Earthquake Early Warning and tsunami modeling will likely lead to increased density of coastal GPS in the near future; under such conditions it becomes more likely for a SSE signal to be captured on multiple instruments and a detection threshold of ~ 2 mm is more reasonable.

For our base model $M_w 6.4$ event (Figure 9; peak slip 72 km offshore), coastal horizontal displacement > 4 mm (peak 9 mm) occurs over ~ 80 km N-S (Table 1). A similar event occurring downdip (Figure S8; peak slip 58 km offshore) of our base model produces coastal horizontal displacement > 4 mm (peak 17 mm) over ~ 100 km N-

S, while a similar updip event (Figure 10; peak slip 100 km offshore) generates no coastal horizontal displacement >4 mm (peak 3 mm). The low stress drop model ($\Delta\sigma_E = 0.014$ MPa; Figure 11) produces coastal horizontal displacement >4 mm (peak 5 mm) over ~ 100 km N-S, and the high stress drop model ($\Delta\sigma_E = 0.217$ MPa; Figure S8) produces <4 mm (peak 10 mm) over ~ 80 km N-S. The M_w 5.9 model (Figure 12) and $\Delta\sigma_E = 0.006$ MPa model (Figure S10) produce a peak 2- and 1-mm coastal horizontal displacement, respectively. The M_w 6.9 model (Figure S9) produces coastal deformation >5 mm (peak 34 mm) over at least 280 km N-S. We would then expect the base, downdip, high, and low stress drop models to produce a resolvable signal, should they occur at a similar latitude to a coastal GPS station. The M_w 6.9 model produces a resolvable GPS signal regardless of its latitude. The updip, M_w 5.9, and $\Delta\sigma_E = 0.006$ MPa models are expected not to be detectable on coastal GPS alone. Thus, our models suggest that a combination of onshore and offshore instrumentation is ideal for the detection of a M_w 6.4 or larger SSE. Further, these models show that any SSE that produces a significant region of resolvable deformation on the continental slope will also produce a resolvable signal on land, suggesting that, from a detection standpoint, it is not necessary to instrument the continental shelf with APGs for the purpose of detecting SSEs of this size. Under the assumption of increased coastal GPS density, all of our modeled SSEs except for the $\Delta\sigma_E = 0.006$ MPa model produce horizontal deformation <2 mm over regions of 50 km N-S or greater and would therefore likely be detectable. Even so, offshore instrumentation would prove valuable in precisely locating and characterizing offshore SSEs to an extent not possible with the limited resolution of purely onshore measurements.

An idealized APG network also has a time-dependent component: the instruments must be active for a sufficient time for a SSE to occur. The M_w 6.4 base event modeled here is expected to recur at a minimum of approximately every 8.4 years, given its peak slip 32 cm, the local convergence rate offshore central Oregon of ~ 3.8 cm/year, and assuming complete strain release by slow slip. This minimum recurrence interval decreases to ~ 7 years in the north of Cascadia and increases to ~ 10.5 years in the south. Our low stress drop model, with a peak slip of 11 cm, is expected to occur no more than every 2.9 years and requires nearly all of the partially locked Oregon segment to rupture. Similarly, lower magnitude SSEs may have lower recurrence intervals but will be more difficult to detect. In the absence of any information as to when and where the last SSE occurred, a decadal-scale instrumentation effort is necessary to determine if and where detectable shallow SSEs occur in Cascadia.

4.4. Slow-Slip Detectability in the CI Experiment

The difficulty of detecting SSEs with the available seafloor pressure data is visualized in Figure 1. The resolvable deformation footprint for the base SSE model covers approximately $4,000 \text{ km}^2$, which represents 15.1% of the approximately $26,500 \text{ km}^2$ between trench and shore offshore central Oregon. The northern segment of this partially locked region was reasonably instrumented in 2011–2012 with five APGs and in 2014–2015 with three APGs provided some coverage for the southern part of the region. This is far fewer instruments than our recommended geometry and the limited instruments present in a given year lacked proximal depth-matched instruments for eliminating oceanographic noise. The 8.4-year recurrence interval of the modeled SSE is longer than the 4-year observational period of the CI experiment and significantly longer than the ~ 1 -year deployment period of a given sensor configuration, so it is unlikely that such an SSE would have occurred while instruments were in place to be able to measure it.

Offshore SSEs identified in other settings (Davis et al., 2015; Wallace et al., 2016) have typically had the advantage of previous datasets, such as onshore GPS or previously recorded tremor, guiding where to deploy instruments and when to look for subtle signals. The Cascadia Subduction Zone is characterized by a wide continental shelf, and there are a wide range of SSE scenarios that would not produce resolvable horizontal deformation on coastal GPS instruments (Table 1). In the absence of any data on shallow SSE occurrence, it is necessary in Cascadia to monitor the entire partially locked Oregon region, requiring a minimum of ~ 20 instruments deployed in a decadal scale experiment to observe a M_w 6.4 or greater event. This geometry could be expanded into a network spanning the entire subduction zone, with an emphasis on those regions with the least constrained locking, namely, the northernmost and southernmost extents of the subduction zone (Schmalzle et al., 2014). Smaller SSEs could be detected with a denser array, but sufficiently small events do not produce any deformation greater than ± 1.5 cm (Figure 12) and would therefore be difficult to detect without improvements in resolution.

5. Conclusions

We show that by utilizing depth-matched differencing, seafloor pressure records are a viable tool for detecting offshore SSEs in Cascadia of similar magnitude to what has been observed at subduction zones globally. Locations at depths from 100 to 250 m require very strict depth matching, within ~10 m, while deeper stations can vary on the order of 1,000-m depth and still achieve significant reductions in RMS. The shallowest available data, though limited, suggest that ≤ 1 -cm RMS cannot be achieved for locations at depths < 100 m. In all cases, the best RMS reduction is achieved by the closest depth matches over separations < 100 km. It is important to test this method in other subduction zone settings, as varying modes of regional circulation may impact the efficacy of depth-matched differencing. Further, Cascadia is a relatively shallow system and we cannot distinguish if the degree of depth matching required is a function of total instrument depth or depth relative to the abyssal plain; it may be that Cascadia is a particularly difficult environment for differencing.

Oceanographic circulation models, though insufficiently accurate to act as a direct correction to pressure records, contain a significant portion of the measured oceanographic signal and are important for understanding the continuity of these pressure signals through the region. These models support the depth difference and separation relationships seen in the APG data, tending to underpredict difference RMS. Because of the temporal heterogeneity of noise in even closely depth-matched differences (lower panels in Figure 4), there is the potential, in using APG data, for misidentifying oceanographic pressure signals as SSEs in the absence of redundant observation of deformation, as these signals manifest similarly in amplitude, duration, and spatial distribution (Figure 13). However, the largest of these such signals are predicted by the oceanographic models, which can be used to avoid their misidentification. As these models are improved in resolution and validation, they will become increasingly useful in assessing the comparability of bottom pressure between locations and may become practical for use as a correction to oceanographic pressure effects.

No offshore SSEs were found in the 4 years of the CI experiment, supplemented by the OOI cabled instruments and an Oregon benchmark, but we determine that the configuration of these APGs was not optimized for the detection of seafloor deformation. A lack of depth-matched stations, the movement of instruments between experiment years, and the limited deployment timeframe restrict the utility of this experiment for SSE detection. Another disadvantage in this setting is that the width of the accretionary prism limits the detectability of offshore slow slip on land-based geodetic networks, so these networks cannot, at their current density, be used to guide seafloor deployments. As such, there is no evidence for an SSE comparable to those observed in Hikurangi and the Japan Trench during this study period.

Our SSE modeling efforts suggest that events with a magnitude comparable to those recorded in other offshore settings could be detected and characterized using 22 APGs arranged in four depth-matched sets, spaced evenly between the trench and shelf break, at 44 km N-S spacing. This is true across a broad range of possible stress drops. Such a system takes advantage of depth-matched instruments to reduce the oceanographic pressure signal to 1 cm RMS or less. Smaller magnitude SSEs could be detected by this system so long as they produce over 1.5 cm of vertical deformation across a region with dimensions on the order of 65 km. However, with decreasing magnitude, low stress drop events will cease to produce a resolvable signal, while high stress drop events will produce resolvable signals only over increasingly small areas. A network capable of detecting small M_w and low stress drop SSEs is impractical unless the deformation detection threshold can be reduced to 1 cm or less. Our oceanographic models and limited depth-matched differences at separations < 100 km suggest that this may be possible, but more observational data are needed to verify this. Even with a 1-cm SSE detection threshold, our modeled areas of significant deformation rapidly fall off with decreasing magnitude, so increasingly dense networks are needed to detect smaller events, which becomes impractical over a regional scale. Improved oceanographic models that more closely predict observed pressures would be valuable in determining the lowest achievable RMS through differencing and thereby determining the smallest possible detectable events using seafloor pressure.

Due to the long recurrence intervals of our modeled SSEs, a consequence of the local convergence rate, any observational network would require a decadal-scale monitoring effort to have a high likelihood of detecting an event. Such a long-term deployment has the added benefit of simplified drift, which becomes stable and linear after several months, allowing for better characterization of signals as non-instrumental. Additionally, our SSE modeling suggests that resolvable horizontal deformation may occur onshore over limited areas for various $M_w > 6.4$ scenarios, so increasing the density of coastal GPS instruments would help better identify

and characterize shallow SSEs in Cascadia. An increase in density would also lower the detection threshold, were a signal to be observed on multiple instruments, enabling the detection of smaller SSEs. The payoff for this observational endeavor would be significant, as the detection and characterization of shallow SSEs in Cascadia may lead to a better understanding of the mechanical properties of the plate boundary and the stress release process leading up to large magnitude megathrust earthquakes.⁴

Acknowledgments

Cascadia Initiative APG data were made possible by the Ocean Bottom Seismograph Instrument Pool (OBSIP; www.obsip.org) and acquired from the Incorporated Research Institutions for Seismology (IRIS; www.iris.edu). Additional APG data came from the Ocean Observatories Initiative (OOI) Cabled Array (www.oceanobservatories.org/array/cabled-array). We thank Laura Wallace and an anonymous reviewer for incisive reviews and Rose Wade and Christian Baillard for useful discussions on the analysis presented herein. This research was supported by NSF grant OCE1558477.

References

- Araki, E., Saffer, D. M., Kopf, A. J., Wallace, L. M., Kimura, T., Machida, Y., et al. (2017). Recurring and triggered slow-slip events near the trench at the Nankai Trough subduction megathrust. *Science*, 356(6343), 1157–1160. <https://doi.org/10.1126/science.aan3120>
- Atwater, B. F. (1987). Evidence for great Holocene earthquakes along the outer coast of Washington State. *Nature*, 236(4804), 942–944. [https://doi.org/10.1126/science.236.4804.944](https://doi.org/10.1126/science.236.4804.942)
- Atwater, B. F., Musumi-Rokkaku, S., Satake, K., Tsuji, Y., Ueda, K., & Yamaguchi, D. K. (2015). *The orphan tsunami of 1700—Japanese clues to a parent earthquake in North America*. U.S. Geological Survey Professional Paper, (2nd ed., Vol. 1707, p. 135). Seattle: University of Washington Press.
- Bletry, Q., Fan, W., Janiszewski, H. A., Lynch, E. M., McCormack, K. A., Phillips, N. J., et al. (2017). Hunting for shallow slow-slip events at Cascadia. In *AGU Fall Meeting Abstracts*.
- Brodsky, E. E., & Mori, J. (2007). Creep events slip less than ordinary earthquakes. *Geophysical Research Letters*, 34, L16309. <https://doi.org/10.1029/2007GL030917>
- Brudzinski, M. R., & Allen, R. M. (2007). Segmentation in episodic tremor and slip all along Cascadia. *Geology*, 35(10), 907–910. <https://doi.org/10.1130/G23740A.1>
- Burgette, R. J., Weldon, R. J., & Schmidt, D. A. (2009). Interseismic uplift rates for western Oregon and along-strike variation in locking on the Cascadia subduction zone. *Journal of Geophysical Research*, 114, B01408. <https://doi.org/10.1029/2008JB005679>
- Chassignet, E. P., Hurlbut, H. E., Smedstad, O. M., Halliwell, G. R., Hogan, P. J., Wallcraft, A. J., et al. (2007). The HYCOM (hybrid coordinate ocean model) data assimilative system. *Journal of Marine Systems*, 65(1), 60–83.
- Collins, C. A., Ivanov, L. M., Melnichenko, O. V., & Garfield, N. (2004). California Undercurrent variability and eddy transport estimated from RAFOS float observations. *Journal of Geophysical Research*, 109, C05028. <https://doi.org/10.1029/2003JC002191>
- Cook, M. J., Sasagawa, G. S., Roland, E. C., Schmidt, D. A., Wilcock, W. S., & Zumberge, M. A. (2017). Campaign-style measurements of vertical seafloor deformation in the Cascadia Subduction Zone using an Absolute Self-Calibrating Pressure Recorder. In *AGU Fall Meeting Abstracts*.
- Cox, C., Deaton, T., & Webb, S. (1984). A deep-sea differential pressure gauge. *Journal of Atmospheric and Oceanic Technology*, 1(3), 237–246. [https://doi.org/10.1175/1520-0426\(1984\)001<0237:ADSDPG>2.0.CO;2](https://doi.org/10.1175/1520-0426(1984)001<0237:ADSDPG>2.0.CO;2)
- Davis, E. E., Villinger, H., & Sun, T. (2015). Slow and delayed deformation and uplift of the outermost subduction prism following ETS and seismogenic slip events beneath Nicoya Peninsula, Costa Rica. *Earth and Planetary Science Letters*, 410, 117–127. <https://doi.org/10.1016/j.epsl.2014.11.015>
- Dixon, T. H., Jiang, Y., Malyservisi, R., McCaffrey, R., Voss, N., Protti, M., & Gonzalez, V. (2014). Earthquake and tsunami forecasts: Relation of slow slip events to subsequent earthquake rupture. *Proceedings of the National Academy of Sciences*, 111(48), 17039–17044. <https://doi.org/10.1073/pnas.1412299111>
- Dragert, G., Wang, K., & James, T. S. (2001). A silent slip event on the deeper Cascadia subduction interface. *Science*, 292(5521), 1236–1058. <https://doi.org/10.1126/science.1060152>
- Emery, W. J., & Thomson, R. E. (2004). *Data analysis methods in physical oceanography*, (2nd ed.p. 638). Amsterdam: Elsevier.
- Fu, Y., & Freymueller, J. T. (2013). Repeated large slow slip events at the southcentral Alaska subduction zone. *Earth and Planetary Science Letters*, 375, 303–311. <https://doi.org/10.1016/j.epsl.2013.05.049>
- Gao, H., Schmidt, D. A., & Weldon, R. J. (2012). Scaling relationships of source parameters for slow slip events. *Bulletin of the Seismological Society of America*, 102(1), 352–360. <https://doi.org/10.1785/0120110096>
- Geng, J., Williams, S. D. P., Teferle, F. N., & Dodson, A. H. (2012). Detecting storm surge loading deformations around the southern North Sea using subdaily GPS. *Geophysical Journal International*, 191(2), 569–578. <https://doi.org/10.1111/j.1365-246X.2012.05656.x>
- Giddings, S. N., MacCready, P., Hickey, B. M., Banas, N. S., Davis, K. A., Siedlecki, S. A., et al. (2014). Hindcasts of potential harmful algal bloom transport pathways on the Pacific Northwest coast. *Journal of Geophysical Research: Oceans*, 119, 2439–2461. <https://doi.org/10.1002/2013JC009622>
- Godin, G. (1972). *The Analysis of Tides*, (p. 264). Toronto: University of Toronto Press.
- Goldfinger, C., Nelson, C. H., Morey, A. E., Johnson, J. E., Patton, J. R., Karabarov, E. B., et al. (2012). Turbidite event history—Methods and implications for Holocene paleoseismicity of the Cascadia Subduction Zone. *U.S. Geological Survey Professional Paper 1661-F*.
- Gomberg, J., Wech, A., Creager, K., Obara, K., & Agnew, D. (2016). Reconsidering earthquake scaling. *Geophysical Research Letters*, 43, 6243–6251. <https://doi.org/10.1002/2016GL069967>
- Hall, K., Houston, H., & Schmidt, D. (2018). Spatial comparisons of tremor and slow slip as a constraint on fault strength in the northern Cascadia Subduction Zone. *Geochemistry, Geophysics, Geosystems*, 19, 2706–2718. <https://doi.org/10.1029/2018GC007694>
- Hirose, H., Hirahara, K., Kimata, F., Fujii, N., & Miyazaki, S. (1999). A slow thrust slip event following the two 1996 Hyuganada earthquakes beneath the Bungo Channel, southwest Japan. *Geophysical Research Letters*, 26(21), 3237–3240. <https://doi.org/10.1029/1999GL010999>
- Hughes, C. W., Williams, J., Blaker, A., Coward, A., & Stepanov, V. (2018). A window on the deep ocean: The special value of ocean bottom pressure for monitoring the large-scale, deep-ocean circulation. *Progress in Oceanography*, 161, 19–46. <https://doi.org/10.1016/j.pocean.2018.01.011>
- Hyndman, R. D. (2013). Down-dip landward limit of Cascadia great earthquake rupture. *Journal of Geophysical Research: Solid Earth*, 118, 5530–5549. <https://doi.org/10.1002/jgrb.50390>
- Inazu, D., Hino, R., & Fujimoto, H. (2012). A global barotropic ocean model driven by synoptic atmospheric disturbances for detecting seafloor vertical displacement from in situ ocean bottom pressure measurements. *Marine Geophysical Research*, 33(2), 127–148. <https://doi.org/10.1007/s11001-012-9151-7>
- Ito, Y., Hino, R., Kido, M., Fujimoto, H., Osada, Y., Inazu, D., et al. (2013). Episodic slow slip events in the Japan subduction zone before the 2011 Tohoku-Oki earthquake. *Tectonophysics*, 600, 14–26. <https://doi.org/10.1016/j.tecto.2012.08.022>

- Jeppson, T. N., Tobin, H. J., & Hashimoto, Y. (2018). Laboratory measurements quantifying elastic properties of accretionary wedge sediments: Implications for slip to the trench during the 2011 Mw 9.0 Tohoku-Oki earthquake. *Geosphere*, 14(4), 1411–1424. <https://doi.org/10.1130/GES01630.1>
- Kato, A., Obara, K., Igarashi, T., Tsuruoka, H., Nakagawa, S., & Hirata, N. (2012). Propagation of slow slip leading up to the 2011 Mw 9.0 Tohoku-Oki Earthquake. *Science*, 335(6069), 705–708. <https://doi.org/10.1126/science.1215141>
- Kurapov, A. L., Erofeeva, S. Y., & Myers, E. (2017). Coastal sea level variability in the US West Coast Ocean Forecast System (WCOFS). *Ocean Dynamics*, 67(1), 23–36. <https://doi.org/10.1007/s10236-016-1013-4>
- Kvalseth, T. O. (1985). Cautionary note about R₂. *The American Statistician*, 39(4), 279–285.
- Lowry, A. R., Larson, K. M., Kostoglodov, V., & Bilham, R. (2001). Transient fault slip in Guerrero, southern Mexico. *Geophysical Research Letters*, 28(19), 3753–3756. <https://doi.org/10.1029/2001GL013238>
- McCrory, P. A., Blair, J. L., Waldhauser, F., & Oppenheimer, D. H. (2012). Juan de Fuca slab geometry and its relation to Wadati-Benioff zone seismicity. *Journal of Geophysical Research*, 117, B09306. <https://doi.org/10.1029/2012JB009407>
- Muramoto, T., Ito, Y., Inazu, D., Wallace, L. M., Hino, R., Suzuki, S., et al. (2019). Seafloor crustal deformation on ocean bottom pressure records with nontidal variability corrections: Application to Hikurangi Margin, New Zealand. *Geophysical Research Letters*, 46, 303–310. <https://doi.org/10.1029/2018GL080830>
- Noda, H., Lapusta, N., & Kanamori, H. (2013). Comparison of average stress drop measures for ruptures with heterogeneous stress change and implications for earthquake physics. *Geophysical Journal International*, 193(3), 1691–1712. <https://doi.org/10.1093/gji/ggt074>
- Nordman, M., Virtanen, H., Nyberg, S., & Mäkinen, J. (2015). Non-tidal loading by the Baltic Sea: Comparison of modelled deformation with GNSS time series. *GeoResJ*, 7, 14–21. <https://doi.org/10.1016/j.grj.2015.03.002>
- Obara, K. (2002). Nonvolcanic deep tremor associated with subduction in southwest Japan. *Science*, 296(5573), 1679–1681. <https://doi.org/10.1126/science.1070378>
- Obara, K., & Kato, A. (2016). Connecting slow earthquakes to huge earthquakes. *Science*, 353(6296), 253–257. <https://doi.org/10.1126/science.aaf1512>
- Ozawa, S., Suito, H., & Tobita, M. (2007). Occurrence of quasi-periodic slow-slip off the east coast of the Boso peninsula, central Japan. *Earth, Planets and Space*, 59(12), 1241–1245. <https://doi.org/10.1186/BF03352072>
- Polster, A., Fabian, M., & Villinger, H. (2009). Effective resolution and drift of Paroscientific pressure sensors derived from long-term seafloor measurements. *Geochemistry, Geophysics, Geosystems*, 10, Q08008. <https://doi.org/10.1029/2009GC002532>
- Porrill, R. W., Allen, R. M., Boyarko, D. C., & Brudzinski, M. R. (2011). Investigation of Cascadia segmentation with ambient noise tomography. *Earth and Planetary Science Letters*, 309(1–2), 67–76. <https://doi.org/10.1016/j.epsl.2011.06.026>
- Radiguet, M., Cotton, F., Vergnolle, M., Campillo, M., Valette, B., Kostoglodov, V., & Cotte, N. (2011). Spatial and temporal evolution of a long term slow slip event: the 2006 Guerrero Slow Slip Event. *Geophysical Journal International*, 184(2), 816–828. <https://doi.org/10.1111/j.1365-246X.2010.04866.x>
- Radiguet, M., Perfettini, H., Cotte, N., Gualandi, A., Valette, B., Kostoglodov, V., et al. (2016). Triggering of the 2014 Mw 7.3 Papanoa earthquake by a slow slip event in Guerrero, Mexico. *Nature Geoscience*, 9(11), 829–833. <https://doi.org/10.1038/ngeo2817>
- Rogers, G., & Dragert, H. (2003). Episodic tremor and slip on the Cascadia Subduction zone: The chatter of silent slip. *Science*, 300(5627), 1942–1943. <https://doi.org/10.1126/science.1084783>
- Ruiz, S., Metois, M., Fuenzalida, A., Ruiz, J., Leyton, F., Grandin, R., et al. (2014). Intense foreshocks and a slow slip preceded the 2014 Iquique Mw 8.1 earthquake. *Science*, 345(6201), 1165–1169. <https://doi.org/10.1126/science.1256074>
- Scherwath, M., Spence, G., Obana, K., Kodaira, S., Wang, K., Riedel, M., et al. (2011). Seafloor seismometers monitor northern Cascadia earthquakes. *Eos*, 92(47), 421–422. <https://doi.org/10.1029/2011EO470001>
- Schmalzle, G. M., McCaffrey, R., & Creager, K. C. (2014). Central Cascadia subduction zone creep. *Geochemistry, Geophysics, Geosystems*, 15, 1515–1532. <https://doi.org/10.1002/2013GC005172>
- Schwartz, S. Y., & Rokosky, J. M. (2007). Slow slip events and seismic tremor at circum-Pacific subduction zones. *Reviews of Geophysics*, 45, RG3004. <https://doi.org/10.1029/2006RG000208>
- Shchepetkin, A. F., & McWilliams, J. C. (2005). The regional oceanic modeling system (ROMS): a split-explicit, free-surface, topography-following-coordinate oceanic model. *Ocean Modelling*, 9(4), 347–404. <https://doi.org/10.1016/j.ocemod.2004.08.002>
- Shelly, D. R., Beroza, G. C., & Ide, S. (2007). Non-volcanic tremor and low-frequency earthquake swarms. *Nature*, 446(7133), 305–307. <https://doi.org/10.1038/nature05666>
- Smith, L. M., Cowles, T. J., Vaillancourt, R. D., Smith, B. L. M., & Cowles, T. J. (2018). Introduction to the special issue on the Ocean Observatories Initiative. *Oceanography*, 31(1), 12–15.
- Stone, H. B., Banas, N. S., & MacCready, P. (2018). The effect of alongcoast advection on Pacific Northwest shelf and slope water properties in relation to upwelling variability. *Journal of Geophysical Research: Oceans*, 123, 265–286. <https://doi.org/10.1002/2017JC013174>
- Stone, I., Vidale, J. E., Han, S., & Roland, E. (2018). Catalog of offshore seismicity in Cascadia: Insights into the regional distribution of microseismicity and its relation to subduction processes. *Journal of Geophysical Research: Solid Earth*, 123, 641–652. <https://doi.org/10.1002/2017JB014966>
- Szeliga, W., Melbourne, T., Santillan, M., & Miller, M. (2008). GPS constraints on 34 slow slip events within the Cascadia subduction zone, 1997–2005. *Journal of Geophysical Research*, 113, B04404. <https://doi.org/10.1029/2007JB004948>
- Thomas, A. L. (1993). Poly3D: A three-dimensional, polygonal element, displacement discontinuity boundary element computer program with applications to fractures, faults, and cavities in the Earth's crust. M.S. Thesis, Stanford University, Stanford, CA.
- Tian, Y. (2011). Nontectonic signals in reprocessed continuous GPS position time series of CMONOC. *Geo-Spatial Information Science*, 14(3), 207–215. <https://doi.org/10.1007/s11806-011-0547-3>
- Tolman, H. L. (2009). User manual and system documentation of WAVEWATCH-III version 3.14. *National Oceanic and Atmospheric Administration*, 276, 220. <https://doi.org/10.3390/jerph2006030011>
- Toomey, D., Allen, R., Barclay, A., Bell, S., Bromirski, P., Carlson, R., et al. (2014). The Cascadia Initiative: A sea change in seismological studies of subduction zones. *Oceanography*, 27(2), 138–150. <https://doi.org/10.5670/oceanog.2014.49>
- Uchida, N., Inuma, T., Nadeau, R. M., Bürgmann, R., & Hino, R. (2016). Periodic slow slip triggers megathrust zone earthquakes in northeastern Japan. *Science*, 351(6272), 488–492. <https://doi.org/10.1126/science.aad3108>
- Vallée, M., Nocquet, J. M., Battaglia, J., Font, Y., Segovia, M., Régnier, M., et al. (2013). Intense interface seismicity triggered by a shallow slow slip event in the Central Ecuador subduction zone. *Journal of Geophysical Research: Solid Earth*, 118, 2965–2981. <https://doi.org/10.1002/jgrb.50216>
- Wallace, L. M., & Beavan, J. (2010). Diverse slow slip behavior at the Hikurangi subduction margin, New Zealand. *Journal of Geophysical Research*, 115, B12A02. <https://doi.org/10.1029/2010JB007717>

- Wallace, L. M., Beavan, J., Bannister, S., & Williams, C. (2012). Simultaneous long-term and short-term slow slip events at the Hikurangi subduction margin, New Zealand: Implications for processes that control slow slip event occurrence, duration, and migration. *Journal of Geophysical Research*, 117, B11402. <https://doi.org/10.1029/2012JB009489>
- Wallace, L. M., Webb, S. C., Ito, Y., Mochizuki, K., Hino, R., Henrys, S., et al. (2016). Slow slip near the trench at the Hikurangi subduction zone, New Zealand. *Science*, 352(6286), 701–704. <https://doi.org/10.1126/science.aaf2349>
- Wang, K., Dragert, H., Kao, H., & Roeloffs, E. (2008). Characterizing an “uncharacteristic” ETS event in northern Cascadia. *Geophysical Research Letters*, 35, L15303. <https://doi.org/10.1029/2008GL034415>
- Wang, K., & Tréhu, A. M. (2016). Invited review paper: Some outstanding issues in the study of great megathrust earthquakes—The Cascadia example. *Journal of Geodynamics*, 98, 1–18. <https://doi.org/10.1016/j.jog.2016.03.010>
- Watts, D. R., & Kontoyiannis, H. (1990). Deep-ocean bottom pressure measurement: Drift removal and performance. *Journal of Atmospheric and Oceanic Technology*, 7(2), 296–306. [https://doi.org/10.1175/1520-0426\(1990\)007<0296:DOBPMD>2.0.CO;2](https://doi.org/10.1175/1520-0426(1990)007<0296:DOBPMD>2.0.CO;2)
- Wech, A. G., & Creager, K. C. (2011). A continuum of stress, strength and slip in the Cascadia subduction zone. *Nature Geoscience*, 4(9), 624–628. <https://doi.org/10.1038/ngeo1215>
- Yamashita, Y., Yakiwara, H., Asano, Y., Shimizu, H., Uchida, K., Hirano, S., et al. (2015). Migrating tremor off southern Kyushu as evidence for slow slip of a shallow subduction interface. *Science*, 348(6235), 676–679. <https://doi.org/10.1126/science.aaa4242>